Chemical Geology 254 (2008) 175–196

Contents lists available at ScienceDirect

Chemical Geology

journal homepage: www.elsevier.com/locate/chemgeo

High-resolution dating of granite petrogenesis and deformation in a lower crustal shear zone: Athabasca granulite terrane, western Canadian Shield

Gregory Dumond [a,*], Noah McLean [b], Michael L. Williams [a], Michael J. Jercinovic [a], Samuel A. Bowring [b]

[a] Department of Geosciences, University of Massachusetts, Amherst, Massachusetts, 01003-9297, USA
[b] Department of Earth, Atmospheric, and Planetary Sciences, Massachusetts Institute of Technology, Cambridge, Massachusetts, 02139, USA

ARTICLE INFO

Article history:
Accepted 24 April 2008

Keywords:
Monazite
Zircon
Granite
Continental crust
Shear zone
Transpression

ABSTRACT

The Athabasca granulite terrane represents >20,000 km^2 of continental lower crust exposed in the hanging wall of the ca. 1.85 Ga thrust–sense Legs Lake shear zone in the western Canadian Shield. The terrane and the thrust zone are cut by the Grease River shear zone. The structure hosts a syn-tectonic granite dike with a high-precision ID-TIMS zircon $^{207}Pb/^{206}Pb$ crystallization age of 1922.6±0.4 Ma (MSWD=3.1, 2σ). Detailed textural analysis and in situ electron probe microanalysis (EPMA) of monazite in the dike indicate three discrete episodes of strain accumulation, each corresponding to syn-kinematic growth of monazite. The results provide evidence for a previously unrecognized >100 m.y. episodic record of sub-horizontal NW–SE shortening and dextral shear strain along the Grease River shear zone. High-Ca domains in ca. 1.92–1.90 Ga monazite are linked to protracted high-*T* strain (ca. 650–700 °C) at lower crustal depths (ca. 1.0 GPa) and correlated with indentation of the Slave craton along the Great Slave Lake shear zone. Syn-kinematic overgrowths of low-Ca monazite+apatite are interpreted as products of deformation-enhanced dissolution and re-precipitation of monazite at 1846±9 Ma (MSWD=1.1, 2σ). The third generation of syn-kinematic monazite yield ca. 1.8 Ga ages. The dataset constrains, for the first time, coeval movement along the strike–slip Grease River shear zone and the thrust–sense Legs Lake shear zone during ca. 1.85 Ga dextral transpression and uplift of continental lower crust to middle crustal levels (ca. 0.5 GPa). Circa 1.8 Ga syn-kinematic monazite domains in dynamically recrystallized feldspars support brittle–ductile reactivation along the Grease River shear zone at shallower crustal levels, coincident with intra-continental strike–slip strain during culmination of the Trans-Hudson orogeny.

1. Introduction

Constraining the age of deformation events remains a first-order problem in continental tectonics. In particular, the timing and duration of displacement along crustal-scale faults and shear zones is fundamental for understanding how plates accommodate large magnitudes of strain during continental collision and extension (e.g. Murphy and Copeland, 2005). Variably deformed granitic rocks in shear zones are sensitive "markers" for dating deformation and understanding crustal rheology for several reasons: 1) shear zones are dynamic environments for strain localization (Berthé et al., 1979), fluid flow (e.g. Mancktelow, 2006), and interaction between metamorphism and dynamic recrystallization (e.g. Holyoke and Tullis, 2006a,b); 2) deformation mechanisms during high- to low-temperature strain for quartz, micas, and feldspars are reasonably well-understood (Tullis, 2002); and 3) granitic rocks contain abundant accessory minerals that may be used to elucidate their petrogenetic and geochronologic history (e.g. Montel, 1993; Bea, 1996; Crowley et al., 2005). Crystallization ages of granitic rocks, however, are "relative" age constraints on host rock deformation (i.e. the rocks are pre- or post-tectonic with respect to certain deformation fabrics). Syn-tectonic interpretations of granite emplacement are commonly debatable and problematic (e.g. Paterson and Tobisch, 1988; Paterson et al., 1989). Structural geologists commonly are faced with the same first-order problem: "When did strain accumulate in an absolute sense?"

Geochronologic analysis of fabric-defining major and accessory phases represents a new and rapidly developing frontier for obtaining temporal constraints on continental deformation (e.g. Shaw et al., 2001; Williams and Jercinovic, 2002; Cliff and Meffan-Main, 2003). We propose that monazite provides the missing link for transforming a "relative" dating constraint inferred from granite cross-cutting relationships into an "absolute" age constraint tied directly to granite-host rock deformation. This hypothesis is tested in a deformed granite dike in which zircon and monazite crystallized prior to (or synchronous with) accumulation of dextral shear strain in a lower crustal shear zone. A high-precision ID-TIMS U–Pb zircon date serves as a geochronologic "benchmark" in the crystallization history that is extended by in situ electron probe microanalysis (EPMA) of monazite.

* Corresponding author. Tel.: +1 413 577 0175.
E-mail address: gdumond@geo.umass.edu (G. Dumond).

0009-2541/$ – see front matter © 2008 Elsevier B.V. All rights reserved.
doi:10.1016/j.chemgeo.2008.04.014

A single, cross-cutting and deformed granite dike preserves a previously unrecognized >100 m.y. record of strain accumulation along the Grease River shear zone in the western Canadian Shield. Three discrete episodes of sub-horizontal NW–SE shortening and dextral shear strain occurred during and after ca. 1.923 Ga crystallization of zircon. The deformation episodes correspond to three generations of post-igneous monazite (ca. 1.92–1.9 Ga, 1.85 Ga, and 1.8 Ga), representing syn-kinematic growth at three crustal levels under different petrologic conditions. The study demonstrates the power of multi-technique, multi-accessory phase analysis for elucidating the pre- to syn-tectonic history preserved in deformed granitoids. The results illustrate the high sensitivity of monazite to deformation-enhanced, dissolution and re-precipitation — providing a powerful tool for timing distinct periods of strain, syn-kinematic reaction, and REE-mobility during shear zone evolution.

2. Geologic setting

The western Canadian Shield of North America represents a collage of Archean cratonic provinces, including the Slave, Churchill, Sask, and Superior provinces, separated by Paleoproterozoic orogens and shear zones (Fig. 1a) (Hoffman, 1988; Ansdell et al., 1995; Whitmeyer and Karlstrom, 2007). One of the world's largest and least understood regions of cratonic lithosphere is the western Churchill province (e.g. Hartlaub et al., 2005; van Breeman et al., 2007a). The Great Slave Lake shear zone and the ca. 2.0–1.9 Ga Taltson–Thelon orogen mark the northwestern limit of the western Churchill province (Hoffman, 1987; Ross, 2002). The ca. 1.9–1.8 Ga Trans-Hudson orogen defines the southeastern boundary (Fig. 1a) (Ansdell, 2005; St-Onge et al., 2006).

The Snowbird tectonic zone is a geophysically-defined, NE-trending lineament that separates the western Churchill province into the Rae and Hearne domains (Fig. 1a) (Hoffman, 1988). The geometry of the central portion of the Snowbird tectonic zone, as exposed north of the ca. 1.7 Ga Athabasca Basin (Rainbird et al., 2007), is attributed to offset of the thrust–sense Legs Lake shear zone by the cross-cutting strike–slip Grease River shear zone (Fig. 1b) (Mahan and Williams, 2005). Restoration of ~110 km of post-1.85 Ga strike–slip displacement along the Grease River shear zone reveals >20,000 km^2 of Archean to Paleoproterozoic continental lower crust deformed at 0.8 to >1.5 GPa (~30 to >50-km paleodepths) (Mahan and Williams, 2005), termed the Athabasca granulite terrane (Fig. 1c) (Mahan et al., in press). The terrane is composed of Archean to Paleoproterozoic mafic and felsic granulites and orthogneisses, bounded on its eastern margin by the Legs Lake shear zone (Figs. 1b and 2) (Mahan and Williams, 2005; Martel et al., 2008; Mahan et al., in press). Fundamentally, the exposure represents continental lower crust of the Rae domain thrusted above middle crustal rocks of the Hearne domain (Mahan et al., 2003). The overall geometry is analogous to other crustal-scale, intra-continental thrust systems like the Kapuskasing uplift of the Superior province (Percival and West, 1994) or the Red Bank thrust of Australia (Teyssier et al., 1985).

2.1. Grease River shear zone

The >400 km-long Grease River shear zone (GRsz) is dominated by penetrative NE-striking, steeply NW-dipping (S_2) foliations with shallowly SW-plunging to sub-horizontal stretching and intersection

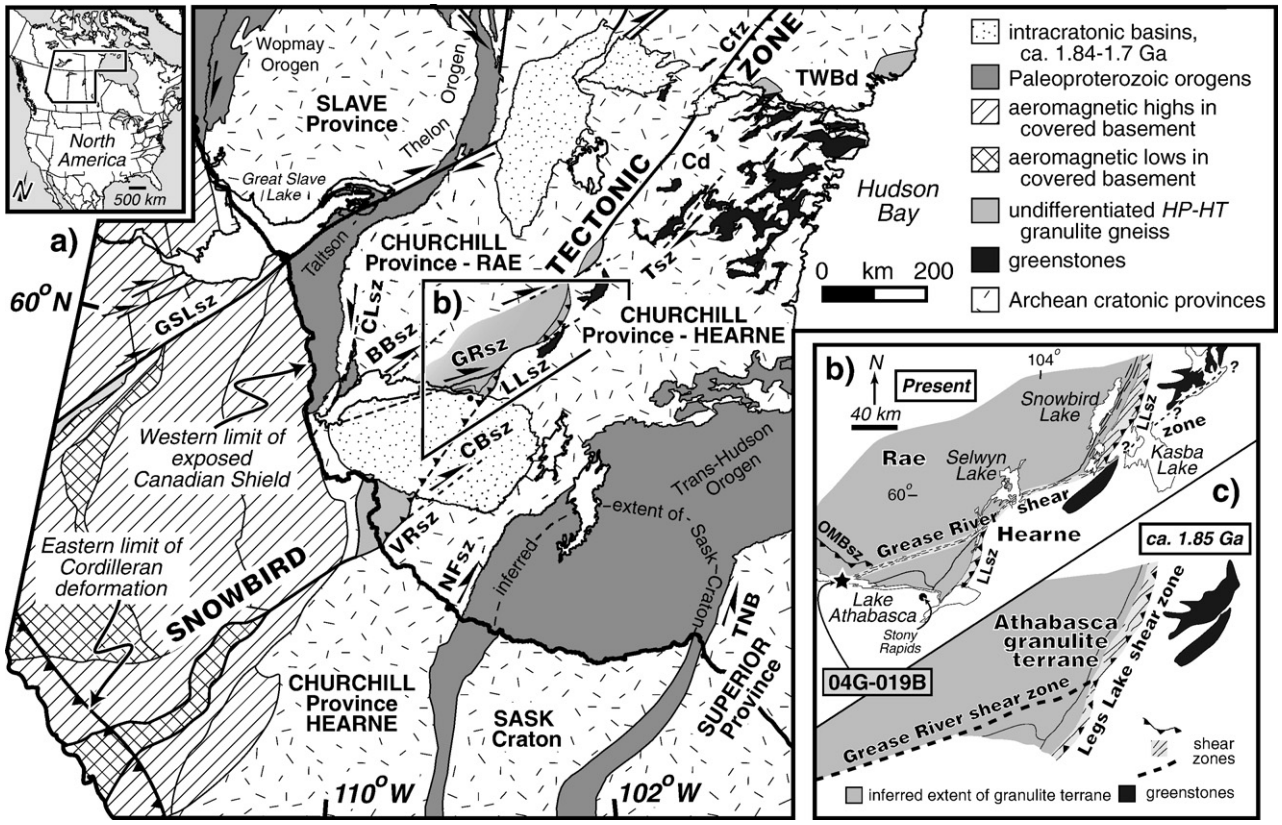

Fig. 1. a) Simplified geologic map of the western Canadian Shield compiled and modified after Hoffman (1988), Tella et al. (2000), Ross (2002), and Hajnal et al. (2005). Note location of inset b) at center. Abbreviations are: GSLsz = Great Slave Lake shear zone; CLsz = Charles Lake shear zone; BBsz = Black Bay shear zone; GRsz = Grease River shear zone; LLsz = Legs Lake shear zone; CBsz = Cable Bay shear zone; VRsz = Virgin River shear zone; NFsz = Needle Falls shear zone; TNB = Thompson Nickel Belt; Tsz = Tyrell shear zone; Cd = Chesterfield domain; Cfz = Chesterfield fault zone (Berman et al., 2007); TWBd = Tehery Wager Bay gneiss domain (van Breeman et al., 2007b). b) Inset depicting present day disposition of Athabasca granulite terrane. Star indicates location of sample 04G-019B in the GRsz. OMBsz = Oldman-Bulyea shear zone. c) Circa 1.85 Ga reconstruction of Athabasca granulite terrane after Mahan and Williams (2005) (compare to Fig. 1b).

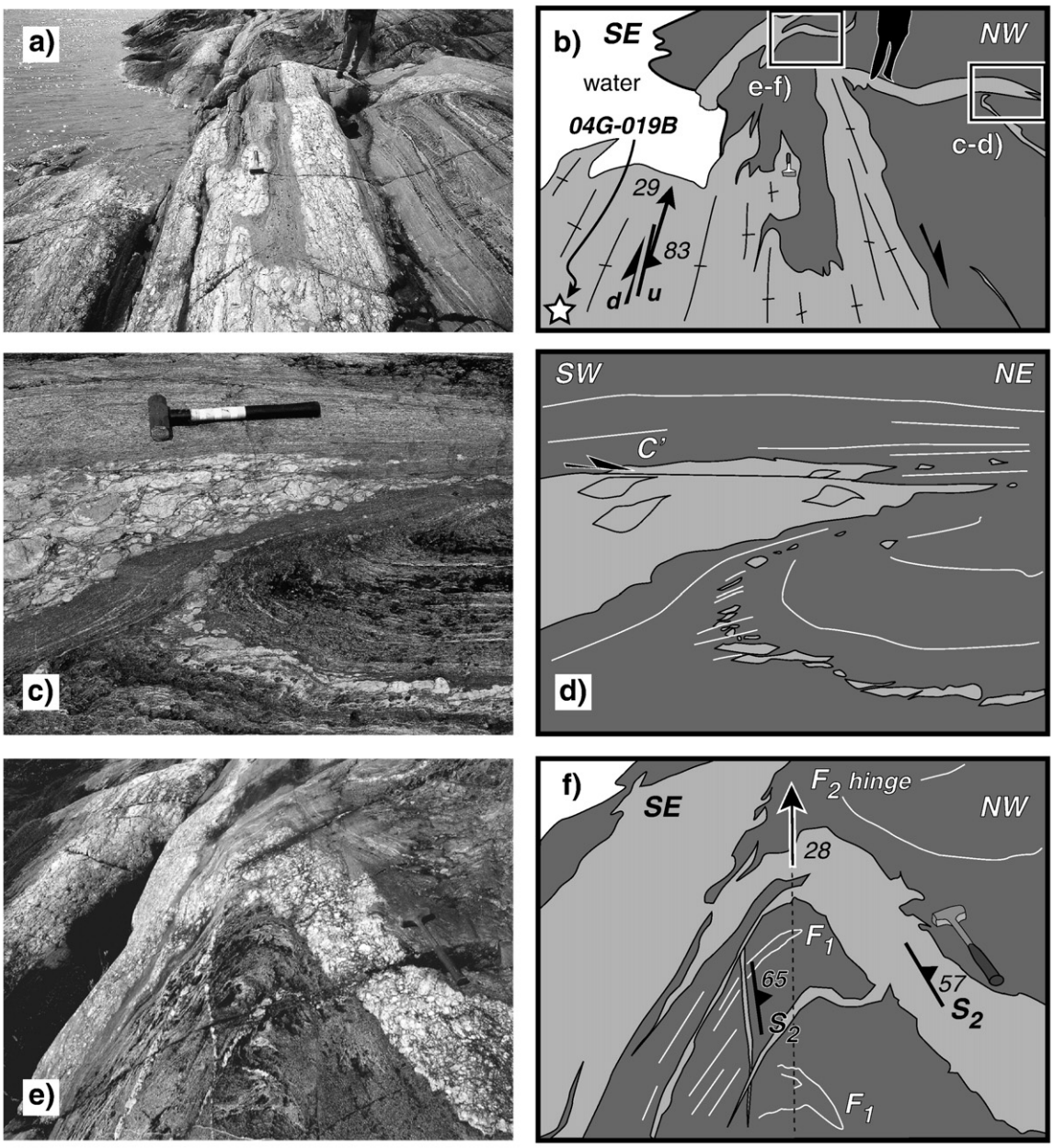

Fig. 2. a–f) Photos and sketches illustrating the field context for dike 04G-019B. a) Image of northwest margin of dike. Southeast margin is underwater. b) Sketch of a) depicting boxed insets that correspond to locations of images/sketches c–d) and e–f). Location (star) of sample 04G-019B is at lower left. Philippe Goncalves of Univeristé de Franche-Comté stands in upper right for scale. c–d) Deformed apophyse of dike and sketch of field observations. Sledge hammer (~30 cm) in c) for scale. Note isolated porphyroclasts derived from the dike in upper right, dextral asymmetry of feldspar porphyroclasts, and C′ shear band. e–f) Photo and sketch of field observations of folded apophyse with smaller apophyses that cut across the F_2 fold at center. Thin apophyse at center is nearly axial-planar to the F_2 fold. Sledge hammer (~30 cm) in e) and f) for scale. Note F_1 fold closures in hinge of F_2 fold and gradient in strain depicted by steepening of S_2 foliation from NW to SE.

lineations (Fig. 1b) (Mahan and Williams, 2005; Dumond et al., 2006; Dumond and Goncalves, unpublished mapping). The western boundary of the ~7 km-wide GRsz is defined by a several km-wide dextral deflection of S_1 gneissic foliation and the onset of a locally intense $L \gg S$-tectonite strain (Dumond and Mahan, unpublished mapping). The eastern boundary of the shear zone coincides with a 0.5–1 km-wide zone of greenschist-facies ultramylonite with local cataclasite and pseudotachylyte (Slimmon, 1989; Hanmer, 1994; LaFrance and Sibbald, 1997; Card, 2001, 2006; Dumond and Goncalves, unpublished mapping, K. Bethune, personal communication). Kinematic indicators in the GRsz include abundant σ- and δ-type feldspar porphyroclasts in tonalitic orthogneisses, C' shear bands and synthetic faults that offset variably deformed dikes, and mantled garnet-porphyroclasts in retrogressed felsic granulites (Dumond et al., 2006; Dumond and Goncalves, unpublished mapping). Kinematics observed throughout the structure are consistent with dextral, dominantly strike–slip displacement with a component of SW-over-NE oblique-thrusting. Thermobarometric data indicate a ca. 0.8–1.1 GPa level (30- to 40-km paleodepth) of continental lower crust exposed at the latitude of Lake Athabasca (Fig. 1b), coincident with the GRsz (Williams et al., 1995, 2000; Dumond et al., 2005; Williams and Hanmer, 2006).

Relatively few geochronologic constraints on the age of shearing along the GRsz have been published prior to this study. Hanmer et al. (1994) reported a U–Pb TIMS zircon crystallization age of 1788 $^{+25}/_{-15}$ Ma from a cross-cutting, deformed leucogranite dike. A ca. 1.8 Ga EPMA date on syn-kinematic rims from one monazite grain

Table 1
Whole rock geochemistry for sample 04G-019B

Oxides		Granite classification		Rare earth elements	
	wt.%[a]	(Frost et al., 2001)			(ppm)[b]
SiO_2	69.65			La	62.7
Al_2O_3	14.32	Al	0.28	Ce	130
Fe_2O_3	1.93	FeO	1.74	Pr	13.7
MnO	0.01			Nd	46
MgO	1.14			Sm	5.14
CaO	1.08	Ca	0.02	Eu	1.27
Na_2O	1.69	Na	0.05	Gd	2.12
K_2O	7.29	K	0.15	Tb	0.11
TiO_2[c]	0.60			Dy	0.22
P_2O_5	0.06	P	0.00	Ho	b.d.
LOI	0.72			Er	0.12
Total	98.50	Fe*	0.60	Yb	b.d.
		MALI	7.90		
		ASI	1.23		

Sample location: UTM E 0383290 N 6577151 Zone 13 NAD 27.
[a] Detection limits (d.l.) for major element oxides = 0.01%.
[b] d.l. for TiO_2 = 0.001%.
[c] d.l. for rare earth elements: La, Ce, Nd = 0.05 ppm. Pr, Sm, Gd, Tb, dy, Ho, Er, and Yb = 0.01. Eu, Tm = 0.005 ppm.

in a felsic granulite ribbon mylonite was presented by Williams and Jercinovic (2002). Dumond et al. (2006) documented ca. 1.9 Ga EPMA dates on syn-kinematic rims from multiple monazite grains in retrogressed felsic granulite gneisses from the eastern boundary of the shear zone. Although the ca. 1.8 Ga record for the GRsz is well-established, the relationship between the GRsz and uplift of the Athabasca granulite terrane along the ca. 1.85 Ga Legs Lake thrust–sense shear zone is unconstrained (Fig. 1b) (Mahan et al., 2006a,b). The pre-1.85 Ga history of the GRsz is poorly understood (Fig. 1c) (i.e. Mahan and Williams, 2005).

2.2. Sample 04G-019B

An oriented sample (04G-019B) was collected from a mylonitized biotite–granite pegmatite dike that was emplaced along, but locally cross-cut early gneissic fabrics (S_1) in the GRsz (Fig. 2). Highly-transposed fragments of similar dikes occur throughout the GRsz, however, the sample location corresponds to the largest and least-transposed outcrop identified in this study (~15–20 m thick). The predominant host rock is a gray, garnet-bearing quartzo-feldspathic gneiss interpreted as a tonalitic orthogneiss. The dike contains a steeply NW-dipping, penetrative foliation (S_2) defined by biotite, tapered and flattened porphyroclasts of plagioclase + K-feldspar (up to 13 cm in length), and mm-scale elongate ribbons of recrystallized quartz + plagioclase + K-feldspar (Fig. 2a and b). Dextral, SW-over-NE kinematics in the dike are defined by σ- and δ-type mantled porphyroclasts of K-feldspar and plagioclase, in addition to well-developed C' shear bands defined by mats of biotite and ribbons of quartz and feldspar (Fig. 2c and d). Apophyses of the dike contain a S_2 axial-planar cleavage and define moderately SW-plunging, open to tight F_2 folds (Fig. 2e and f). The apophyses are locally dismembered and boudinaged in the hinges and limbs of F_2 folds and along outcrop-scale, moderately- to steeply-dipping D_2 thrust zones. The dismemberment is typically manifested as partial to complete isolation of feldspar porphyroclasts from the dike within the host orthogneiss (Fig. 2c and d). Field observations are most consistent with a post-S_1 and pre- to early syn-S_2 relative age for the dike, implying the date of emplacement constrains the age of earliest ductile S_2-strain along the GRsz at this locality.

3. Analytical methods

Whole rock bulk geochemistry for major and rare earth elements was commercially obtained through Activation Laboratories, Ltd. in Ancaster, Ontario, Canada (Table 1). A portion of the sample 04G-019B was crushed and processed utilizing standard heavy mineral separation techniques to obtain a separate of zircon grains for analysis by U–Pb ID-TIMS using the VG Sector 54 mass spectrometer in the Isotope Lab at the Massachusetts Institute of Technology (Table 2). Slabs of the sample were cut perpendicular to foliation and parallel to the stretching lineation to identify shear sense kinematics and the textural setting of monazite (e.g. Passchier and Trouw, 2005). Two ~30 μm-thick polished thin-sections (04G-019B-1 and 04G-019B-2) were commercially prepared from the slabs for optical petrography and in situ EPMA. Backscattered electron (BSE) imaging, X-ray mapping, and quantitative analyses of monazite were done using the Cameca® SX50 and Cameca® "Ultrachron" electron microprobes

Table 2
ID-TIMS U–Pb zircon data for sample 04G-019B

	Composition		Isotope ratios								Dates (Ma)						
Fraction	$^{206}Pb^*/Pb_c$[a]	Pb_c (pg)[b]	$^{206}Pb/^{204}Pb_c$[c]	$^{206}Pb/^{238}U$[d]	% error (2σ)[e]	$^{207}Pb/^{235}U$[d]	% error (2σ)[e]	$^{207}Pb/^{206}Pb$[d]	% error (2σ)[e]	Corr. coef	$^{206}Pb/^{238}U$[f]	± (2σ)	$^{207}Pb/^{235}U$[f]	± (2σ)	$^{207}Pb/^{206}Pb$[f]	± (2σ)	% disc[g]
XL13a	2703	0.65	49,638	0.346912	0.088	5.634706	0.112	0.117801	0.040	0.948	1919.84	1.45	1921.42	0.96	1923.13	0.72	0.17
XL13b	387	0.42	24,417	0.347389	0.154	5.640131	0.169	0.117753	0.040	0.973	1922.12	2.56	1922.25	1.46	1922.40	0.72	0.01
XL13c	138	0.34	37,555	0.346929	0.054	5.634572	0.088	0.117793	0.040	0.952	1919.92	0.90	1921.40	0.76	1923.00	0.72	0.16
XL13d	154	1.16	9504	0.346937	0.056	5.636112	0.090	0.117822	0.041	0.947	1919.96	0.93	1921.64	0.78	1923.46	0.74	0.18
XXL11a	596	0.68	169,610	0.346930	0.071	5.634360	0.099	0.117788	0.040	0.943	1919.92	1.19	1921.37	0.86	1922.93	0.72	0.16
XXL11b	787	1.17	46,284	0.346677	0.060	5.625539	0.094	0.117690	0.045	0.920	1918.71	1.00	1920.02	0.81	1921.43	0.81	0.14
XXL11c	3341	2.04	8159	0.347100	0.103	5.636750	0.127	0.117780	0.051	0.925	1920.74	1.70	1921.74	1.10	1922.82	0.91	0.11
XXL11d	302	3.60	6762	0.345062	0.178	5.603514	0.192	0.117777	0.043	0.976	1910.98	2.95	1916.64	1.66	1922.77	0.77	0.61
L02a	2758	0.93	32,827	0.345760	0.068	5.613992	0.097	0.117760	0.040	0.942	1914.32	1.12	1918.25	0.84	1922.50	0.72	0.43
L02b	768	1.04	18,917	0.346948	0.139	5.631243	0.155	0.117717	0.041	0.967	1920.01	2.30	1920.89	1.34	1921.85	0.73	0.10
L02c	1281	0.23	168,720	0.347371	0.054	5.648174	0.087	0.117927	0.040	0.953	1922.03	0.89	1923.48	0.75	1925.04	0.71	0.16
XXL13a	119	0.27	208,078	0.346221	0.100	5.625026	0.121	0.117834	0.040	0.953	1916.53	1.65	1919.94	1.05	1923.63	0.72	0.37
XXL13b	1991	0.39	127,989	0.345952	0.092	5.615420	0.115	0.117724	0.040	0.950	1915.24	1.53	1918.47	0.99	1921.96	0.72	0.35
XXL13c	521	0.33	79,104	0.346289	0.060	5.621179	0.092	0.117730	0.040	0.946	1916.85	1.00	1919.35	0.79	1922.05	0.72	0.27

[a] Ratio of radiogenic Pb (including ^{208}Pb) to common Pb. All common Pb is assumed to be laboratory blank.
[b] Total weight of common Pb (including ^{208}Pb).
[c] Measured ratio corrected for fractionation and spike.
[d] Corrected for fractionation, spike, and laboratory blank.
[e] Errors propagated using the algorithms of Schmitz and Schoene (2007).
[f] Calculations are based on the decay constants of Jaffey et al. (1971).
[g] % discordance = 100 − (100 × ($^{206}Pb/^{238}U$ date ÷ $^{207}Pb/^{206}Pb$ date)).

in the Electron Microprobe/SEM Facility at the University of Massachusetts — Amherst (Fig. 3 and Table 3).

3.1. Zircon geochronology by ID-TIMS

Approximately 75 zircon grains from the mineral separate were transferred into a covered quartz crucible and annealed by heating to 900 °C for 60 h in a muffle furnace. Zircon grains were recovered from the crucible and mounted in a 1-inch epoxy cylinder that was polished to reveal grain interiors. Grains were imaged utilizing a cathodoluminescence (CL)-detector mounted on the JEOL Superprobe 733 at the Massachusetts Institute of Technology. Zircon grains were chosen for analysis with the goal of minimizing Pb loss and metamict zones inferred from complex CL-zoning. Many zircon grains contained thin (tens of μm) CL-bright rims, attributed to post-emplacement metamorphic overgrowth. Four grains were plucked from the epoxy mount and air-abraded with pyrite following the method of Krogh (1982) to remove the rims. Each grain was broken into multiple fragments prior to a 12-hour partial dissolution step in 29 M HF at 180 °C to remove radiation-damaged components (i.e. "chemical abrasion" of Mattinson, 2005).

The zircon fragments were ultrasonically cleaned and fluxed for ~1 h in 3 M nitric acid after chemical abrasion. Fragments were rinsed in ultrapure acetone and water, loaded into 300 μL Teflon FEP microcapsules, and spiked with a mixed ^{205}Pb–^{233}U–^{235}U tracer. The fragments were dissolved at 210 °C for 48 h in ~75 μL of 29 M HF and ~25 μL of ~5 M HNO_3 and dried to fluorides. Re-dissolution of fragments occurred in ~50 μL of 6 M HCl for 12 h at 180 °C. U and Pb were isolated using HCl-based single-column anion exchange chemistry with AG1×8 resin (modified after Krogh, 1973) and then loaded together in a silica gel 0.1 M H_3PO_4 emitter solution on single Re filaments.

U and Pb isotopic measurements were performed on a VG Sector 54 multi-collector TIMS (Table 2). For all but one sample, Pb was analyzed with a dynamic Faraday–Daly routine. The routine provides real-time Daly gain correction by alternating between: 1) placing mass 204 in the Daly detector and masses 205–208 in Faraday collectors, and 2) placing mass 205 in the Daly and masses 206–208 in the Faradays collectors. Fraction XL13a was run by peak-hopping on the Daly detector. Pb isotopic fractionation was measured at 0.25+/−0.04%/amu on the Daly detector and 0.07+/−0.04%/amu on the Faraday detectors via long-term analysis of standard NBS-981. U was measured in static Faraday mode, with fractionation determined in real-time using the ^{233}U–^{235}U double-spike. All analytical data were calculated based on the decay constants of Jaffey et al. (1971) with errors propagated using the algorithms of Schmitz and Schoene (2007).

3.2. Monazite geochronology and trace element analysis by EPMA

Monazite Th–U–total Pb geochronology by EPMA in this study follows the strategy proposed by Williams et al. (2006). Full-section X-ray maps of thin-sections 04G-019B-1 and -2 were collected via EPMA to identify all monazite grains (Fig. 4a; Appendix A; Williams and Jercinovic, 2002). Five grains were mapped at high-spatial resolution (0.3–6.0 μm) (Figs. 3b and 7a). For brevity, all monazite grains are referred to hereafter by their section and grain number (i.e. 1-m2, 1-m4, 1-m5, 1-m8, and 2-m1). X-ray maps were processed simultaneously (Fig. 8) and individually (Fig. 9a) to identify similar and texturally distinct compositional domains to guide subsequent quantitative analysis (Williams et al., 2006).

All quantitative trace element analyses were preceded by high-resolution wavelength spectral scans and peak overlap corrections following the methods of Jercinovic and Williams (2005) and Jercinovic et al. (2008-this issue) (see also Pyle et al., 2005). All background scans and quantitative analyses were carried out with a focused beam at 15 kV and 200 nA using a modified Cameca® SX100 electron microprobe — the Cameca® "Ultrachron" EPMA. Details regarding the instrument, analytical protocol, and standards used are summarized in Appendix A and Fig. 3 (see also Jercinovic et al., 2008-this issue). Acceptance or rejection of analytical points was guided by high-resolution X-ray maps and BSE imaging of each analyzed grain (e.g. Fig. 3b and c). Analyses that overlapped domain boundaries or cracks were excluded. Data points collected nearest to the point of background acquisition in a domain were selected over points analyzed furthest away. Locations of quantitative data in post-acquisition BSE images were compared with X-ray maps to exclude points that fell on compositional gradients (Fig. 3c). Potential over- or underestimations of background intensities were evaluated through multiple regressions and picks of the WDS (wavelength-dispersive spectrometer) scans.

The determination of the "domain-specific" date and error follows Williams et al. (2006). The 2σ uncertainty on the date reported for each domain includes: 1) an estimate of short-term random error obtained by propagating uncertainties for Th, U, and Pb through the age equation, and 2) a component of short-term systematic error derived from an estimated 1% uncertainty on the regressed models of the background intensities (Williams et al., 2006). The final result is illustrated as a single Gaussian probability distribution for each monazite domain (Fig. 3c). Multiple domains from one or more grains (interpreted to represent the same monazite growth event based on similarity in date, composition, and/or texture) were grouped together using a weighted mean age with 2σ uncertainty (Fig. 11a) (e.g. all ca. 1.85 Ga high-Y rims linked to garnet breakdown in Mahan et al., 2006a). Multiple results from a consistency standard of known age are presented along with the data to document short-term systematic error and provide a qualitative assessment of accuracy during the analytical session (Williams et al., 2006). The results are plotted as histograms scaled relative to the consistency standard (Figs. 3c and 11a). The consistency standard used in this study is the Moacyr Brazilian pegmatite monazite with weighted mean ages of 506±1 (2σ, MSWD=0.6) for $^{208}Pb/^{232}Th$, 506.7±0.8 Ma (2σ, MSWD=0.83) for $^{207}Pb/^{235}U$, and 515.2±0.6 Ma (2σ, MSWD=0.36) for $^{206}Pb/^{238}U$ obtained by ID-TIMS at the Geological Survey of Canada (W.J. Davis, personal communication). Eight sets of analyses (1 set=4–8 analytical points) were collected periodically during two multi-day analytical sessions and yielded a weighted mean date of 505±2 Ma (Fig. 3c).

4. Results

Sample 04G-019B is a megacrystic, porphyroclast-rich augen granite with plagioclase+K-feldspar+quartz and rusty, orange-brown biotite as major phases. Plagioclase is anti-perthitic with mm-scale patchy domains of K-feldspar (Fig. 4a). Feldspars display variable alteration to K-bearing white mica, e.g. sericite (Fig. 3a). Accessory phases in decreasing abundance include rutile+monazite+apatite. Zircon was not identified in thin-section. Vitreous-brown, prismatic rutile occurs as aligned, elongate grains (up to 200 μm in length) associated with biotite and quartz in the foliation and in strain shadows with biotite around plagioclase and K-feldspar. Apatite occurs as small grains (10 s of μm or less in diameter) disseminated throughout the matrix foliation, in poly-crystalline mantles adjacent to dynamically recrystallized feldspar porphyroclasts, and as inclusions in biotite. Apatite is commonly associated with microfractures in plagioclase and K-feldspar (e.g. Fig. 4c), and always occurs in contact with monazite.

Major element whole rock geochemistry indicates that the granite dike is alkali–calcic (MALI=7.90), magnesian (Fe*=0.6), and peraluminous (ASI=1.23) (after the classification of Frost et al., 2001; see Table 1). The bulk composition is similar to many peraluminous leucogranites and Cordilleran granitoids (Chacko et al., 2000; Frost et al., 2001), with a low-Ca character suitable for monazite

Table 3
EPMA monazite major and trace element data for sample 04G-019B[a]

Point	Domain	Element (wt.% oxide)																	Mole fraction[b]					Cations (per formula unit) on the basis of 4 oxygens						
		CaO	SiO_2	P_2O_5	AS_2O_3	La_2O_3	Ce_2O_3	Nd_2O_3	Pr_2O_3	Sm_2O_3	Gd_2O_3	Eu_2O_3	Tm_2O_3	Y_2O_3	ThO_2	UO_2	PbO	Total	X_{Hut}	X_{Che}	X_{LaPO_4}	X_{SmPO_4}	$X_{La/Sm}$	Ca	Si	P	As	La	Ce	Nd
1	7	0.27	1.22	28.46	b.d.	15.19	32.33	11.98	3.27	0.43	0.56	0.68	0.15	0.10	4.77	0.13	0.43	99.95	0.0749	0.0064	0.2152	0.0061	35	0.012	0.049	0.958	b.d.	0.223	0.471	0.170
2	8	0.43	0.79	29.62	b.d.	17.52	30.37	9.87	2.77	0.14	0.33	0.63	0.10	0.06	4.12	0.03	0.34	97.12	0.0639	0.0108	0.2618	0.0022	122	0.018	0.031	0.999	b.d.	0.257	0.443	0.140
3	2	1.24	0.63	29.23	b.d.	13.10	29.34	11.88	3.09	0.46	0.50	0.63	0.15	0.11	7.28	0.09	0.65	98.38	0.1057	0.0301	0.1906	0.0067	28	0.053	0.025	0.988	b.d.	0.193	0.429	0.170
4	2	1.08	0.70	29.54	b.d.	13.14	28.90	11.72	3.00	0.42	0.47	0.60	0.12	0.08	6.72	0.05	0.59	97.14	0.1001	0.0269	0.1958	0.0063	31	0.046	0.028	0.999	b.d.	0.193	0.423	0.167
5	3	1.11	0.79	29.50	b.d.	13.15	28.78	11.43	3.04	0.32	0.51	0.61	0.11	0.10	7.33	0.11	0.65	97.54	0.1102	0.0277	0.1949	0.0048	41	0.048	0.032	0.996	b.d.	0.194	0.420	0.163
6	1	1.11	0.51	29.47	b.d.	13.46	29.25	11.63	3.07	0.42	0.50	0.61	0.16	0.10	6.26	0.09	0.56	97.18	0.0923	0.0276	0.1997	0.0063	32	0.048	0.021	1.000	b.d.	0.199	0.429	0.167
7	1	1.09	0.58	29.75	0.62	13.63	30.28	12.22	3.17	0.45	0.52	0.66	0.14	0.09	6.57	0.08	0.59	100.45	0.0944	0.0263	0.1955	0.0066	30	0.046	0.023	0.987	0.015	0.197	0.435	0.171
8	2	1.24	0.64	29.38	b.d.	12.94	28.75	11.74	3.06	0.45	0.43	0.61	0.17	0.10	7.39	0.10	0.66	97.66	0.1089	0.0305	0.1908	0.0068	28	0.053	0.026	0.994	b.d.	0.191	0.421	0.167
9	3	1.01	0.77	29.39	b.d.	14.03	30.13	11.91	3.10	0.34	0.51	0.63	0.15	0.11	6.96	0.09	0.61	99.74	0.1015	0.0242	0.2010	0.0049	41	0.043	0.031	0.982	b.d.	0.204	0.435	0.168
10	3	0.97	0.87	29.35	b.d.	14.08	30.50	12.04	3.22	0.42	0.46	0.65	0.09	0.10	7.07	0.14	0.64	100.61	0.1036	0.0230	0.1992	0.0060	33	0.041	0.034	0.979	b.d.	0.204	0.439	0.169
11	1	1.08	0.51	29.54	b.d.	13.73	29.50	11.58	3.12	0.38	0.51	0.60	0.09	0.10	6.15	0.09	0.55	97.53	0.0905	0.0268	0.2029	0.0056	36	0.046	0.021	0.999	b.d.	0.202	0.431	0.165
12	2	1.19	0.61	29.31	b.d.	13.00	28.94	11.67	3.05	0.46	0.63	0.63	0.15	0.11	7.08	0.09	0.63	97.55	0.1044	0.0294	0.1915	0.0069	28	0.051	0.024	0.994	b.d.	0.192	0.424	0.167
13	3	1.21	0.58	29.70	b.d.	14.73	30.38	11.49	3.07	0.31	0.52	0.62	0.15	0.11	6.98	0.10	0.62	100.57	0.0987	0.0289	0.2089	0.0044	47	0.051	0.023	0.986	b.d.	0.213	0.436	0.161
14	3	1.12	0.86	29.35	b.d.	14.24	29.89	11.61	3.15	0.35	0.56	0.61	0.11	0.10	7.69	0.16	0.70	100.49	0.1121	0.0266	0.2019	0.0051	40	0.047	0.034	0.977	b.d.	0.206	0.430	0.163
15	6	0.26	2.75	27.00	b.d.	14.49	29.59	11.24	3.02	0.23	0.44	0.61	0.11	0.05	10.84	0.07	0.90	101.60	0.1659	0.0060	0.2003	0.0032	63	0.011	0.109	0.909	b.d.	0.213	0.431	0.160
16	2	1.14	0.66	30.29	0.64	13.68	30.05	12.33	3.15	0.40	0.37	0.63	0.10	0.10	6.95	0.08	0.62	101.20	0.0997	0.0273	0.1960	0.0058	34	0.047	0.026	0.991	0.015	0.195	0.425	0.170
17	4	1.14	0.53	29.42	b.d.	13.99	30.94	11.72	3.07	0.44	0.46	0.66	0.17	0.11	6.57	0.11	0.58	99.89	0.0935	0.0271	0.1995	0.0063	32	0.048	0.021	0.982	b.d.	0.204	0.447	0.165
18	5	0.48	1.37	28.14	b.d.	14.04	29.72	11.53	3.09	0.35	0.45	0.64	0.18	0.07	6.89	0.08	0.57	97.60	0.1082	0.0117	0.2053	0.0051	40	0.021	0.056	0.964	b.d.	0.210	0.441	0.167
19	5	0.48	1.30	28.03	0.38	14.25	30.78	12.20	3.30	0.42	0.52	0.66	0.14	0.10	6.57	0.11	0.57	99.81	0.1008	0.0115	0.2024	0.0060	34	0.021	0.052	0.951	0.009	0.211	0.452	0.175
20	8	0.46	1.39	28.29	b.d.	13.98	29.54	11.67	3.14	0.39	0.48	0.65	0.15	0.09	6.75	0.10	0.58	97.66	0.1068	0.0113	0.2047	0.0058	35	0.020	0.056	0.967	b.d.	0.208	0.437	0.168
21	7	0.25	1.75	27.79	b.d.	14.66	30.89	11.98	3.22	0.27	0.54	0.66	0.13	0.06	7.15	0.10	0.61	100.05	0.1118	0.0059	0.2068	0.0038	55	0.011	0.070	0.941	b.d.	0.216	0.452	0.171
22	4	1.08	0.65	29.21	b.d.	13.34	29.10	11.47	3.00	0.37	0.52	0.60	0.14	0.12	6.61	0.17	0.61	96.98	0.1003	0.0268	0.1980	0.0055	36	0.046	0.026	0.993	b.d.	0.198	0.428	0.165
Moacyr 07-03-07		0.48	1.36	28.13	b.d.	14.32	29.20	11.29	3.06	1.03	0.89	0.64	0.21	1.44	7.33	0.08	0.16	99.61	0.1054	0.0114	0.2036	0.0148	14	0.020	0.054	0.950	b.d.	0.211	0.426	0.161
Moacyr 07-04-07		0.48	1.35	28.31	b.d.	13.66	27.72	10.79	2.94	1.01	0.96	0.65	0.17	1.43	7.37	0.08	0.17	97.08	0.1103	0.0118	0.2020	0.0150	13	0.021	0.055	0.968	b.d.	0.203	0.410	0.156
Moacyr 07-04-07-2		0.48	1.41	28.67	b.d.	13.71	27.83	10.83	2.98	1.05	0.95	0.63	0.17	1.44	7.33	0.06	0.16	97.71	0.1090	0.0119	0.2021	0.0156	13	0.021	0.056	0.969	b.d.	0.202	0.407	0.154
Moacyr 07-04-07-3		0.46	1.39	28.38	b.d.	14.61	29.66	11.52	3.10	1.02	0.83	0.64	0.19	1.43	7.18	0.07	0.16	100.63	0.1022	0.0108	0.2056	0.0145	14	0.020	0.055	0.951	b.d.	0.213	0.430	0.163
Moacyr 07-05-07		0.46	1.41	28.90	b.d.	14.39	29.33	11.31	3.11	0.96	0.97	0.65	0.19	1.45	7.15	0.07	0.16	100.49	0.1027	0.0109	0.2045	0.0138	15	0.019	0.055	0.961	b.d.	0.208	0.422	0.159
Moacyr 07-06-07		0.47	1.40	28.80	b.d.	14.47	29.16	11.34	3.12	0.96	1.02	0.66	0.23	1.46	7.23	0.07	0.16	100.54	0.1035	0.0112	0.2052	0.0137	15	0.020	0.055	0.957	b.d.	0.209	0.419	0.159
Moacyr 07-10-07		0.46	1.43	28.30	b.d.	14.04	29.37	11.23	3.11	0.97	0.99	0.66	0.23	1.43	7.28	0.06	0.16	99.74	0.1049	0.0109	0.2000	0.0140	14	0.020	0.057	0.954	b.d.	0.206	0.428	0.160
Moacyr 07-11-07		0.46	1.42	28.33	b.d.	14.42	30.31	11.56	3.12	1.05	0.91	0.68	0.18	1.43	7.26	0.06	0.16	101.37	0.1022	0.0108	0.2008	0.0148	15	0.019	0.056	0.945	b.d.	0.210	0.438	0.163

[a] Tb, Dy, Ho, Er, and Yb were analyzed and found below detection (b.d. = below detection).

[b] Mole fractions for components of monazite calculated after Pyle et al. (2001).

[c] With the exception of Y, Th, U, and Pb, all elements are reported as simple means. Values for Y, Th, U, and Pb are reported as weighted means with the error based on propagation of the standard deviation of the mean of the X-ray counting uncertainties (for '*n*' analyses) plus 1% uncertainty on the estimated background intensities through the age equation of Montel et al. (1996).

[d] Dates calculated after Williams et al. (2006). Uncertainties on the decay constants for ^{232}Th, ^{238}U, and ^{235}U are not included.

Table 3 (*continued*)

Point	Domain	Cations (per formula unit) on the basis of 4 oxygens													Y (ppm)[c]	PropEr	Th (ppm)[c]	PropEr	U (ppm)[c]	PropEr	Pb (ppm)[c]	PropEr	Date[d]	
		Pr	Sm	Gd	Eu	Tm	Y	Th	U	Pb	∑	La+Ce	REE+Y+Si	Ca+P	WtAv	2σ	WtAv	2σ	WtAv	2σ	WtAv	2σ	2σ	*n*
1	7	0.047	0.006	0.007	0.009	0.002	0.002	0.043	0.001	0.005	1.057	0.693	0.986	0.970	795	44	41831	154	1110	32	3963	16	1854±17	6 of 7
2	8	0.040	0.002	0.004	0.009	0.001	0.001	0.037	0.000	0.004	0.997	0.700	0.930	1.017	495	58	36181	192	257	22	3112	22	1805±25	3 of 4
3	2	0.045	0.007	0.007	0.009	0.002	0.002	0.067	0.001	0.007	2.003	0.622	0.888	1.041	857	52	64014	276	800	30	5996	24	1922±18	4 of 7
4	2	0.044	0.005	0.006	0.008	0.001	0.002	0.061	0.000	0.006	1.991	0.616	0.879	1.045	651	60	59058	296	473	26	5448	28	1924±21	3 of 6
5	3	0.044	0.005	0.007	0.008	0.001	0.002	0.066	0.001	0.007	1.993	0.614	0.876	1.043	789	46	64050	248	956	28	5997	22	1906±16	4 of 7
6	1	0.045	0.006	0.007	0.008	0.002	0.002	0.057	0.001	0.006	1.997	0.628	0.885	1.048	770	44	54972	196	799	26	5203	18	1928±15	6 of 7
7	1	0.045	0.006	0.007	0.009	0.002	0.002	0.059	0.001	0.006	2.009	0.632	0.896	1.033	688	52	57777	252	714	28	5445	24	1934±18	4 of 9
8	2	0.045	0.006	0.006	0.009	0.002	0.002	0.067	0.001	0.007	1.995	0.611	0.874	1.047	817	54	64937	280	840	30	6084	26	1920±18	4 of 7
9	3	0.045	0.005	0.007	0.009	0.002	0.002	0.063	0.001	0.007	2.002	0.639	0.907	1.025	849	60	61187	306	757	34	5688	28	1909±21	3 of 5
10	3	0.046	0.006	0.006	0.009	0.001	0.002	0.063	0.001	0.007	2.008	0.644	0.919	1.019	811	60	62165	310	1227	42	5960	28	1918±21	3 of 5
11	1	0.046	0.005	0.007	0.008	0.001	0.002	0.056	0.001	0.006	1.995	0.634	0.888	1.045	786	52	54065	238	752	30	5118	22	1932±19	4 of 7
12	2	0.045	0.006	0.008	0.009	0.002	0.002	0.064	0.001	0.007	1.997	0.616	0.879	1.045	886	62	62247	312	805	34	5833	28	1920±21	3 of 7
13	3	0.044	0.004	0.007	0.008	0.002	0.002	0.062	0.001	0.007	2.007	0.650	0.901	1.037	885	52	61346	266	889	32	5773	24	1918±18	4 of 7
14	3	0.045	0.005	0.007	0.008	0.001	0.002	0.069	0.001	0.007	2.003	0.637	0.902	1.024	825	52	67554	290	1377	36	6469	26	1912±18	4 of 10
15	6	0.044	0.003	0.006	0.008	0.001	0.001	0.098	0.001	0.010	2.005	0.644	0.977	0.920	392	58	95182	462	598	22	8333	36	1842±17	3 of 10
16	2	0.044	0.005	0.005	0.008	0.001	0.002	0.061	0.001	0.006	2.003	0.620	0.883	1.038	818	44	61114	216	676	22	5710	20	1927±15	6 of 11
17	4	0.044	0.006	0.006	0.009	0.002	0.002	0.059	0.001	0.006	2.003	0.651	0.906	1.030	873	60	57701	290	948	38	5422	28	1903±22	3 of 6
18	5	0.046	0.005	0.006	0.009	0.002	0.002	0.064	0.001	0.006	1.998	0.650	0.941	0.985	583	60	60515	304	730	32	5283	26	1801±20	3 of 5
19	5	0.049	0.006	0.007	0.009	0.002	0.002	0.060	0.001	0.006	2.012	0.663	0.963	0.972	749	52	57767	252	976	34	5252	24	1842±19	4 of 7
20	8	0.046	0.006	0.007	0.009	0.002	0.002	0.062	0.001	0.006	1.996	0.645	0.940	0.987	695	52	59291	258	824	30	5364	24	1848±18	4 of 6
21	7	0.047	0.004	0.007	0.009	0.002	0.001	0.065	0.001	0.007	2.004	0.669	0.980	0.952	445	50	62555	270	826	30	5640	24	1850±18	4 of 8
22	4	0.044	0.005	0.007	0.008	0.002	0.003	0.060	0.002	0.007	1.994	0.626	0.885	1.040	940	48	58132	226	1488	36	5653	22	1908±17	5 of 7
Moacyr 07-03-07		0.045	0.014	0.012	0.009	0.003	0.031	0.067	0.001	0.002	1.061	0.637	0.965	0.970	11348	80	64413	196	661	18	1506	10	503±5	8 of 8
Moacyr 07-04-07		0.043	0.014	0.013	0.009	0.002	0.031	0.068	0.001	0.002	1.032	0.613	0.936	0.988	11355	84	64462	210	532	18	1488	12	500±6	7 of 7
Moacyr 07-04-07-2		0.043	0.014	0.012	0.009	0.002	0.031	0.067	0.001	0.002	1.027	0.609	0.931	0.990	11297	80	64799	198	671	18	1535	10	510±5	8 of 8
Moacyr 07-04-07-3		0.045	0.014	0.011	0.009	0.002	0.030	0.065	0.001	0.002	1.062	0.643	0.972	0.970	11232	112	63100	272	595	24	1481	14	507±7	4 of 4
Moacyr 07-05-07		0.045	0.013	0.013	0.009	0.002	0.030	0.064	0.001	0.002	1.046	0.630	0.955	0.980	11403	92	62798	222	579	20	1477	12	508±6	6 of 6
Moacyr 07-06-07		0.045	0.013	0.013	0.009	0.003	0.030	0.065	0.001	0.002	1.049	0.628	0.955	0.977	11467	92	63535	224	573	20	1489	12	506±6	6 of 6
Moacyr 07-10-07		0.045	0.013	0.013	0.009	0.003	0.030	0.066	0.001	0.002	1.057	0.634	0.965	0.974	11290	112	64005	276	557	24	1496	14	506±8	4 of 4
Moacyr 07-11-07		0.045	0.014	0.012	0.009	0.002	0.030	0.065	0.001	0.002	1.071	0.648	0.978	0.965	11239	100	63844	246	568	22	1472	14	499±7	5 of 5

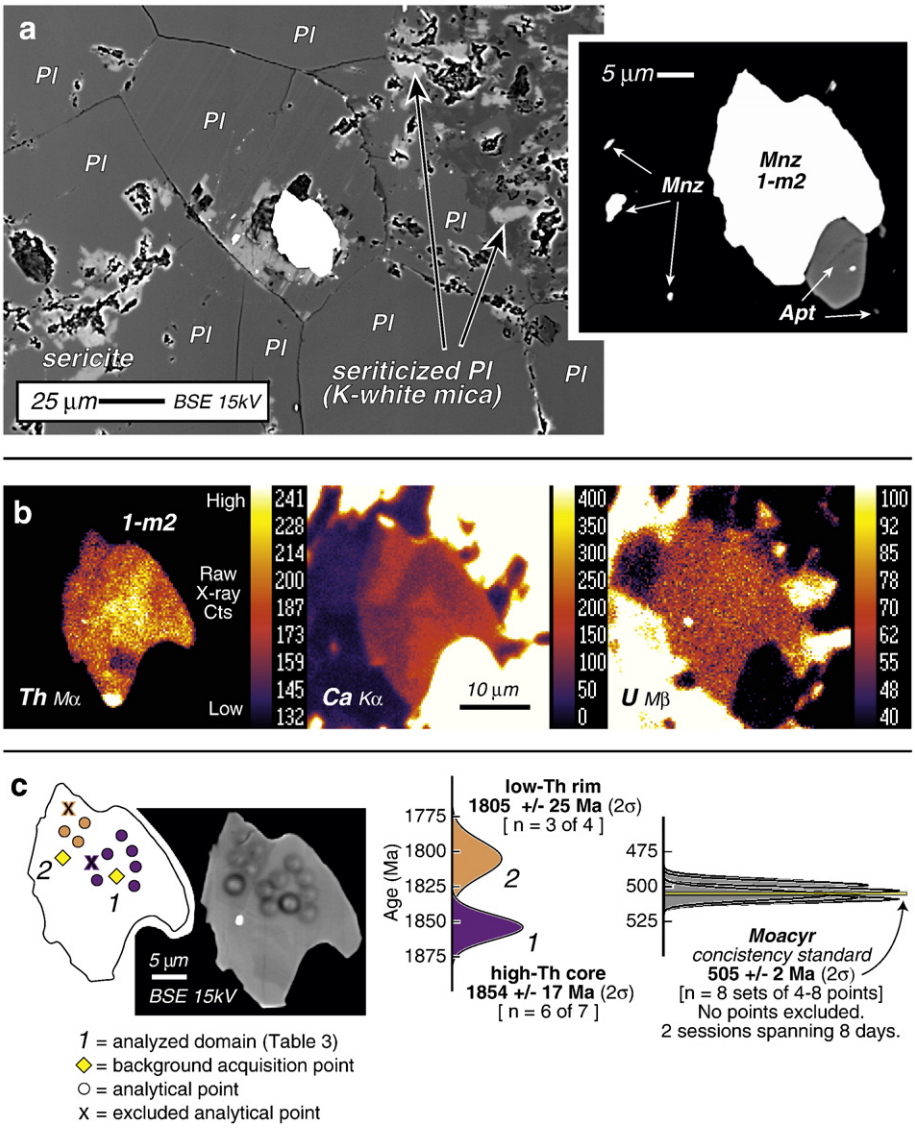

Fig. 3. Technique figure summarizing analytical approach utilized in this study for trace element electron probe microanalysis of monazite. Mineral abbreviations in all figures are after Bucher and Frey (2002). a) Variably optimized high-contrast backscattered electron (BSE) images depict the petrographic setting of grain 04G-019B-1-m2 in the altered, poly-crystalline mantle of a dynamically recrystallized plagioclase porphyroclast. Note adjoining apatite and matrix monazite. b) High spatial-resolution X-ray maps (0.3 µm step size) of Th*Mα*, Ca*Kα*, and U*Mβ* for grain 1-m2. c) Post-acquisition sketch and BSE image of grain 1-m2. Circles represent zones of carbon deposition during background collection and quantitative analysis. Results for grain 1-m2 are plotted as Gaussian distributions that are scaled relative to the Moacyr consistency standard analyzed in this study (see Williams et al., 2006).

crystallization (Montel, 1993). Chondrite-normalized REE data reveal heavy-REE depletions consistent with derivation from a garnet-bearing source (Fig. 5).

4.1. U–Pb ID-TIMS geochronology of zircon separates guided by cathodoluminescence imaging

Four large zircon grains (~200–450 µm in diameter) characterized by well-developed oscillatory- and sector-zoning were chosen to constrain the crystallization age of dike 04G-019B (Fig. 6a). Results from high-precision U–Pb ID-TIMS geochronology consist of 14 separate analyses, each representing a fragment from one of the four abraded zircon grains (see Table 2 and Fig. 6b). Of the 14 analyses, 13 comprise a cluster with a weighted mean $^{207}Pb/^{206}Pb$ date of 1922.6±0.4 Ma (MSWD=3.1), interpreted as the crystallization age of the dike. Fraction L02c has the oldest $^{207}Pb/^{206}Pb$ date of 1925.04±0.71 Ma (2σ) (Table 2). The slightly older date for L02c is most likely due to a small component of inherited zircon, and is not included in the weighted mean. Scatter about the weighted mean is slightly larger than that expected for analytical errors alone, indicating some small component of inheritance, non-zero age Pb loss, and/or a protracted crystallization history. Incomplete removal of overgrowths during air-abrasion may also have contributed to this scatter. The crystallization age is most conservatively constrained between the maximum (1924 Ma) and minimum (1921 Ma) $^{207}Pb/^{206}Pb$ dates (Fig. 6b; Table 2).

4.2. Microstructures and deformation mechanisms in a deformed granite dike

Microstructural observations provide insights into the mechanisms and temperature of deformation that attended production of penetrative gneissic fabric in the granite dike (Fig. 4) (as reviewed by Tullis, 2002). Two microstructural domains are dominant at the thin-section scale (Fig. 4). The first domain consists of core-and-mantle structures defined by K-feldspar and plagioclase porphyroclast cores surrounded by recrystallized poly-crystalline mantles of K-feldspar± plagioclase±quartz (e.g. Passchier and Trouw, 2005) (Fig. 4b and c).

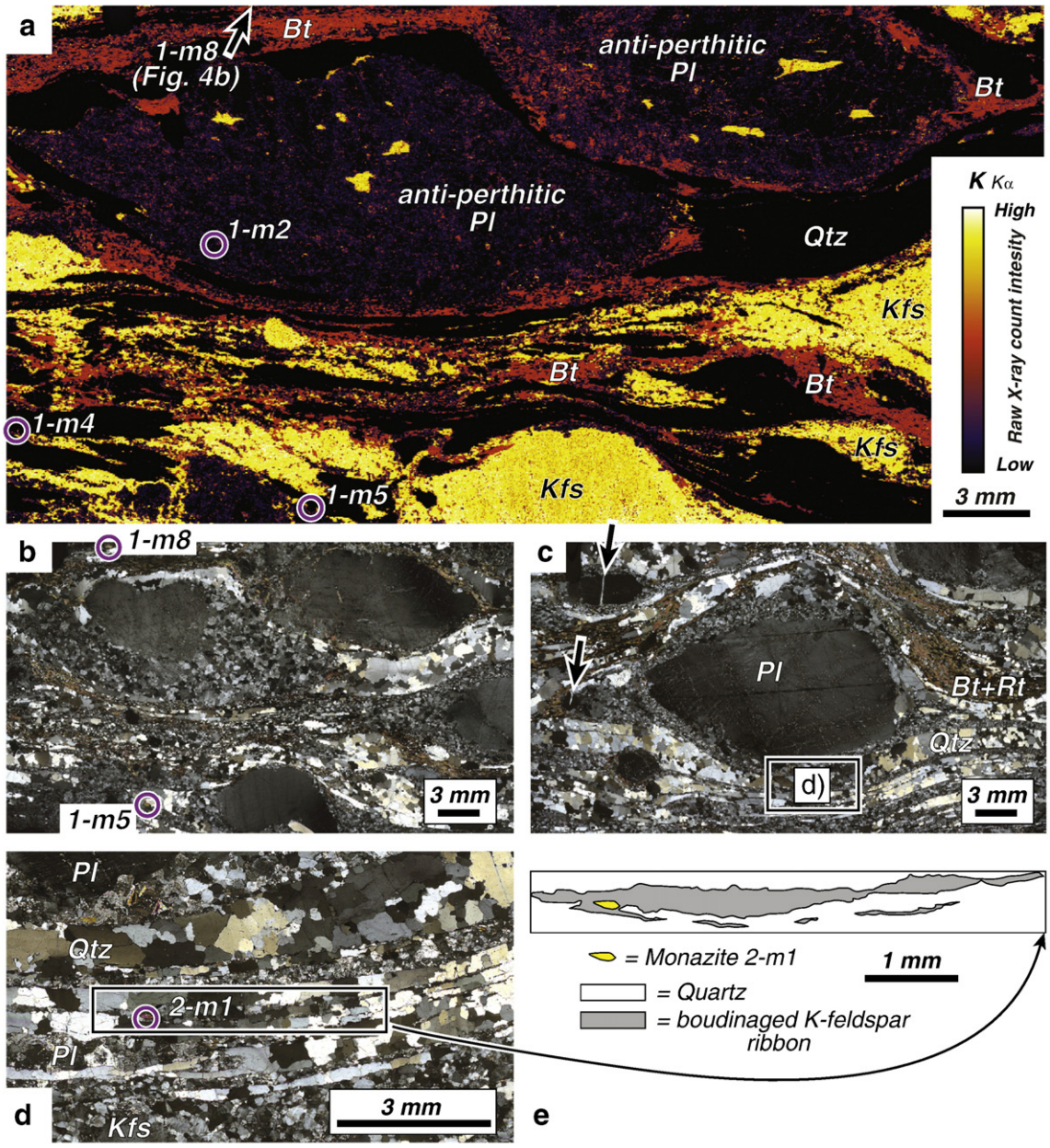

Fig. 4. Microstructural observations from thin-sections 04G-019B-1 and -2. a) Full-section EPMA stage-scan K*Kα* X-ray map depicting the setting of grains 1-m2, 1-m4, 1-m5, and 1-m8. Note large clasts of anti-perthitic plagioclase at top of section and K-feldspar ribbons and clasts at bottom of section. b) Full thin-section cross-polarized light image of 04G-019B-1. Note location of grains 1-m5 and 1-m8 and well-developed core-and-mantle structure in feldspars. c) Full thin-section cross-polarized light image of 04G-019B-2. Note location of grain 2-m1 and inset. Arrows at left point to locations of quartz-filled cracks that cut across cores of plagioclase porphyroclasts. Location of inset d) depicted by box. d) Detail of inset showing ribbon structure in plagioclase and K-feldspar. Note abundant pinning microstructures in quartz and variably-developed lobate grain boundaries in quartz bands. e) Sketch of boudinaged K-feldspar ribbon that hosts grain 2-m1.

Mantles of recrystallized grains, as small as ~10–100 μm in diameter, tend to develop lobate to straight, re-equilibrated boundaries (e.g. Fig. 3a). Recrystallized grains in the mantles are characterized by increasing crystallographic misalignment with increasing distance away from the porphyroclast cores. Biotite commonly forms strain shadows around mantled porphyroclasts (Fig. 4a and c) and locally around monazite (Figs. 7c and 9b).

The second microstructural domain consists of ~0.5–1 mm-thick undulating to straight, mono-mineralic gneissic layers or ribbon structure (e.g. banded mylonite: Tullis, 2002) (Fig. 4c and e). The layers are defined by aggregates of quartz or feldspar grains that locally span the length of the thin-section (Fig. 4c) (e.g. Passchier and Trouw, 2005). Grain boundaries of quartz at the margins of the layers commonly display pinning and window microstructures with biotite and rutile (i.e. Jessell, 1987) (Figs. 4d and 7c). Recrystallized ribbons of K-feldspar and plagioclase (10 s–100 s of μm in thickness) are interlayered with the quartz layers (Fig. 4d and e). The feldspar ribbons exhibit microboudinage (i.e. bulge and thin along the foliation) and locally merge into bifurcated bands of poly-crystalline quartz (Figs. 4e and 7d). K-feldspar and quartz commonly share lobate to cuspate grain boundaries in these domains (see arrows in Fig. 7a, c, and d) (i.e. Gower and Simpson, 1992). Most feldspar and quartz grains display sweeping undulatory extinction and varying amounts of subgrain development with local occurrence of a re-equilibrated foam structure (e.g. Passchier and Trouw, 2005).

The two microstructural styles in 04G-019B are most consistent with the combined operation of subgrain rotation and grain boundary migration recrystallization at high temperature (ca. 650–700 °C).

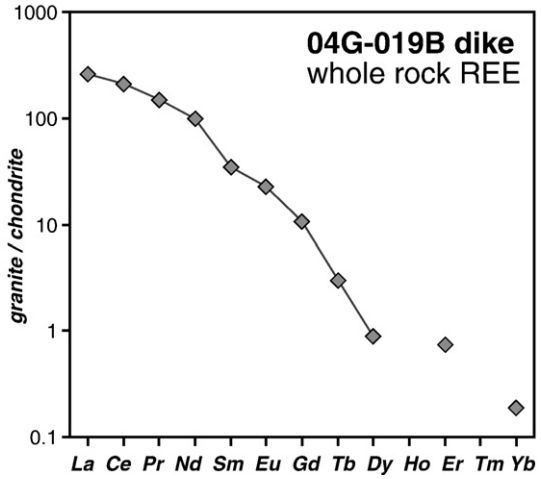

Fig. 5. Chondrite-normalized rare earth element diagram derived from whole rock geochemistry for granite sample 04G-019B. Chondrite values from McDonough and Sun (1995).

Microstructures were overprinted by lower-*T* (ca. 500 °C or less) deformation mechanisms such as undulose extinction in quartz and brittle fracturing of feldspar porphyroclasts (e.g. quartz-filled cracks that cut across plagioclase clasts in Fig. 4c) (see reviews by Tullis, 2002; Passchier and Trouw, 2005).

4.3. Monazite microstructural setting and compositional zoning

Optical petrography, high-contrast BSE imaging, and simultaneously processed high-resolution X-ray maps of monazite for Ca*Kα*, Th*Mα*, and U*Mβ* can be used to delineate microstructural and compositional domains in monazite (Note: maps for Y*Lα* revealed no detectable zoning). Results from the textural/fabric analysis described below (and illustrated in Figs. 3a, b, 4, and 7–9) provide a relative temporal and compositional framework for subsequent trace element and geochronologic analysis (Figs. 10 and 11).

4.3.1. Microstructural setting of monazite

Monazite grains occur in a variety of textures, always in contact with variable amounts of apatite (Figs. 3a and 7). Monazite (~25 to >500 μm in the longest dimension) is commonly hosted by K-feldspar+quartz+ serticitized plagioclase (Figs. 3a and 7). Grains 1-m2 and 2-m1 are completely enclosed by recrystallized feldspars (Figs. 3a and 7d). Grain 1-m2 is located in the fine-grained (as small as 90–100 μm in diameter) recrystallized mantle of a plagioclase porphyroclast (Figs. 3a and 4a). Grain 2-m1 is completely included within a ribbon of K-feldspar between alternating recrystallized gneissic layers of Qtz and feldspar (Figs. 4c, e and 7d). The three remaining matrix grains are mantled by dynamically recrystallized quartz+K-feldspar+plagioclase with minor biotite (Figs. 4a, b and 7a, c).

4.3.2. Compositional zoning in monazite

Simultaneously processed high-resolution X-ray maps define multiple compositional domains in monazite from the Grease River dike. The most fundamental characteristic of nearly all monazite grains is the presence of a high-Ca core in sharp contact with a low-Ca rim (<5–50 μm in width) (Fig. 8a). Comparison of Ca*Kα*, Th*Mα*, and U*Mβ* X-ray maps facilitated subdivision of cores and rims, as described below (Fig. 8).

High-Ca cores are characterized by four domains that locally display oscillatory- and sector-zoning defined by Ca and Th (e.g. 1-m4, 1-m5, and 1-m8 in Fig. 8b). The innermost two core domains are best illustrated by grains 1-m5 and 1-m8, which contain low-Th/low-Ca inner cores that are cross-cut or mantled by oscillatory- and sector-zoned higher Th+Ca outer core domains (Fig. 8a and b). The third high-Ca domain is defined by high-U, Th-enriched outer regions that cut texturally-resorbed compositional zoning defined by Ca and Th in the cores (e.g. grains 1-m4, 1-m5, and 1-m8 in Fig. 8c). These high-U regions have sharp inner contacts that truncate sector-zoned core domains and either grade outward to lower-U (e.g. upper right rim of 1-m5: Fig. 8b and c) or step sharply down to lower-U, Th-depleted outer zones (e.g. bottom rim of 1-m5: Fig. 8b and c). The contacts occur inward of low-Ca rims as observed from the core outward, indicating dissolution and re-precipitation of high-Ca monazite and growth of U-enriched monazite *prior* to growth of low-Ca rim domains (compare Ca*Kα* and U*Mβ* maps for grains 1-m4, 1-m5, and 1-m8 in Fig. 8).

A fourth high-Ca core domain is unique to grain 2-m1 and includes a high-U inner core that is mantled by successive overgrowths defined by Ca and Th (Figs. 8 and 9a). The sketch in Fig. 9a emphasizes the well-developed Ca-zoning in the core truncated by an elongate overgrowth. The high-Ca overgrowth occurs in sharp contact with the resorbed core (Fig. 9a). These attributes suggest that the multi-domain core of 2-m1 is compositionally distinct from the cores of all other grains imaged in Fig. 8.

Zoning in low-Ca rims is variably developed, but four domains can be correlated across all grains imaged in Fig. 8. Three rim domains are delineated in Ca*Kα* maps. Inner low-Ca rim domains occur in contact with high-Ca cores and are separated from outermost rim domains of similar X-ray intensity by lower-Ca monazite (e.g. three low-Ca domains in right rim of 2-m1 in Fig. 8a). Grain 1-m2 is solely characterized by two low-Ca domains with the lowest Th (Fig. 8a and b). Rims of grains 1-m4, 1-m5, and 2-m1 exhibit the same low-Ca domains observed in 1-m2, though with higher apparent Th (Fig. 8a and b). The fourth rim domain is observed in Th*Mα* maps and is unique to grain 1-m8. This domain corresponds to the highest Th in all grains, and is coincident with low-Ca rims and intergrowths (white zones in Fig. 8b).

Fine-grained matrix apatite consistently occurs within and adjacent to low-Ca monazite rims (Figs. 7 and 8a). Apatite grain boundaries truncate zoning in the high-Ca cores and cut across rims (e.g. note location of "white" apatite grains adjacent to 1-m5 and 2-m1 in Fig. 8a). Observations are compatible with growth of apatite after crystallization and resorption of high-Ca monazite (e.g. bottom rim of grain 1-m5; left tip of grain 1-m8; bottom of grain 2-m1: Figs. 7b, d and 8a).

Individual monazite grains and internal compositional sub-domains define shape-preferred orientations that are consistent with the dextral, top-to-the-NE kinematics observed in outcrop (Fig. 2). Locally, grains define "mineral fish" geometries (after Passchier and Trouw, 2005: e.g. single grains 1-m5, 1-m8, 2-m1, and the high-Ca core of 2-m1 in Figs. 4d, 7b–d, 8a, and 9). Maps for high-Ca core domains reveal internal cores and σ-type overgrowths attributed to syn-kinematic growth (e.g. 2-m1: Fig. 9a). Syn-kinematic growth of high-Ca, locally Th- and U-enriched rims is indicated by σ-type overgrowth development (e.g. high-U rims of grains 1-m4 and 1-m5: Fig. 8c). Low-Ca monazite rims also define asymmetric tails illustrative of σ-type porphyroclasts (e.g. 2-m1: Fig. 8a). Locally, high-Ca core domains appear broken and boudinaged with gaps filled by low-Ca monazite (e.g. 1-m8: Figs. 8a and 9b). The right tip of grain 1-m8 is defined by a fragment of high-Ca monazite separated by Th-rich, low-Ca monazite associated with a lobate intergrowth of K-feldspar (Figs. 8a, b and 9b). The texture indicates syn-kinematic growth of low-Ca monazite during fracturing of high-Ca monazite and simultaneous grain boundary migration of K-feldspar (Fig. 9b).

The above observations point to eight texturally and compositionally distinct monazite domains:

- High-Ca Core Domain 1) low-Th+Ca sector- and oscillatory-zoned inner cores (i.e. 1-m5 and 1-m8: Fig. 8a and b),
- High-Ca Core Domain 2) high-Th+Ca sector- and oscillatory-zoned monazite (e.g. 1-m4), locally occurring as outer core domains that cross-cut Domain 1 cores (e.g. 1- m5 and 1-m8: Fig. 8a and b),

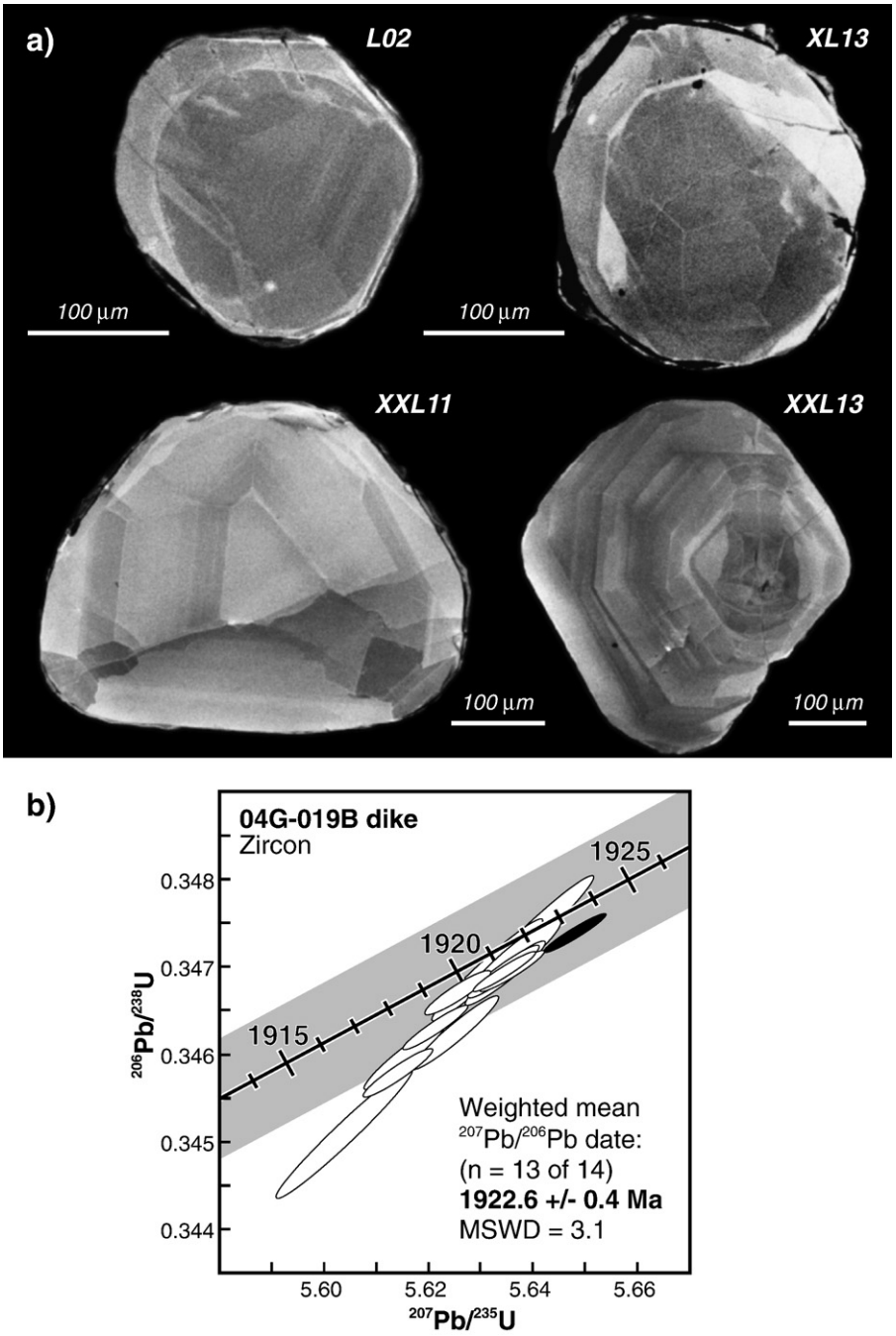

Fig. 6. a) Cathodoluminescence images of analyzed zircon grains separated from dike 04G-019B. Images were collected prior to physical abrasion and fracturing of each grain. b) U–Pb concordia diagram summarizing ID-TIMS zircon data. Gray band represents the concordia curve error envelope using the U decay constants and 95% confidence intervals reported by Jaffey et al. (1971) (see also Schoene et al., 2005).

- High-Ca Core Domain 3) high-U+Th high-Ca monazite that occurs in sharp contact with resorbed, sector- and oscillatory-zoned cores of Domains 1 and 2 (1-m4, 1-m5, and 1-m8: Fig. 8c),
- High-Ca Core Domain 4) anomalously-zoned high-Ca core of grain 2-m1 (Fig. 9a),
- Low-Ca Rim Domain 5) low-Ca+high-Th monazite that separates fractured components of grain 1-m8, occurring in contact with resorbed Domain 3 (Figs. 8b and 9b),
- Low-Ca Rim Domain 6) low-Ca monazite in sharp contact with resorbed high-Ca Domains 3 and 4 (1-m4, 1-m5, 1-m8, and 2-m1: Fig. 8a),
- Low-Ca Rim Domain 7) lower-Ca zones in sharp contact with Domain 6 low-Ca rims (1-m2, left tip of 1-m5, and right tip 2-m1: Fig. 8a), and
- Low-Ca Rim Domain 8) higher-Ca outermost tips and rims in sharp contact with Domain 7 and the matrix (i.e. 1-m2, 1-m5, and 2-m1: Fig. 8a).

4.4. Monazite geochemistry

Major and trace element abundances in monazite obtained by EPMA are presented in Table 3 and illustrated in Fig. 10. Numbered data points in Fig. 10 correspond to the locations of analyzed domains in Figs. 3c and 11. Mole fractions for monazite components are calculated after Pyle et al. (2001). All domains are Y-depleted (~400–1000 ppm: Table 3), in contrast to Y-rich monazite from high-grade pelitic bulk compositions (e.g. Pyle and Spear, 2003; Gibson et al., 2004). Compositional variation in monazite is predominantly controlled by

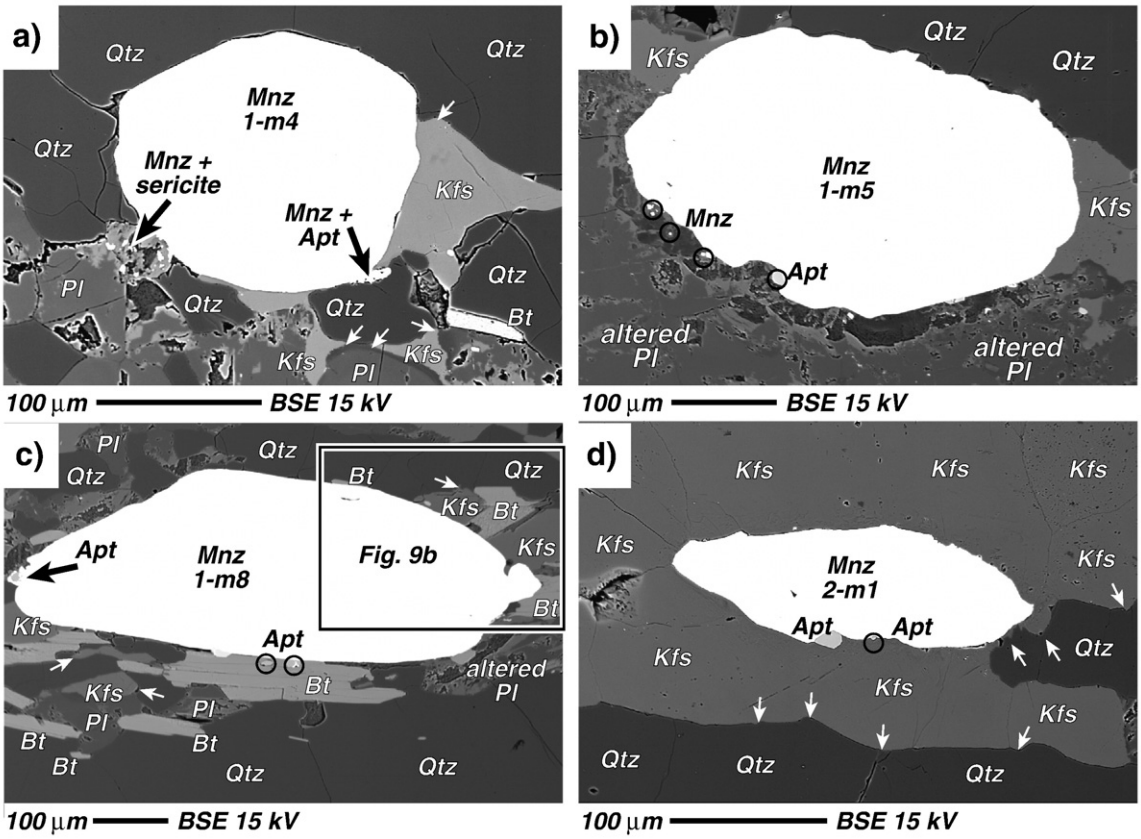

Fig. 7. Backscattered electron images illustrating microstructures and textural setting of monazite grains a) 1-m4, b) 1-m5, c) 1-m8, and d) 2-m1. White arrows point to cuspate-lobate grain boundaries between K-feldspar and quartz ± plagioclase. Black arrows and circles highlight locations of apatite. Further details for grain 1-m2 appear in Fig. 3. Inset in Fig. 7c shows location of Fig. 9b.

coupled substitutions involving Th, Ca, Si, and/or P and the rare earth elements (Gramaccioli and Segalstad, 1978; reviews by Zhu and O'Nion, 1999; Spear and Pyle, 2002; Williams et al., 2007), i.e.:

$$2REE^{3+} \leftrightarrow Th^{4+} + Ca^{2+} \text{(cheralite or "brabantite")} \quad (1)$$

and

$$REE^{3+} + P^{5+} \leftrightarrow Th^{4+} + Si^{4+} \text{(huttonite)}. \quad (2)$$

Monazite compositions and exchange vectors for reactions (1) and (2) are illustrated in Fig. 10a. The influence of these substitution mechanisms is readily illustrated by plotting the Ca-dependent mole fraction components in Fig. 10b, revealing the contrast between Ca-rich monazite (e.g. cheralite-rich Domains 1–4) and Ca-poor monazite (e.g. cheralite-poor Domains 5–8) (Fig. 8a). High-Ca Domain 1 inner core zones are generally depleted in both huttonite and cheralite components, relative to Domain 2 outer core regions (Fig. 10b).

The association of monazite + apatite (e.g. Fig. 7) has been observed naturally and reproduced experimentally via fluid–mineral interaction and coupled substitutions (Pan and Fleet, 2002; Harlov et al., 2005), including:

$$P^{5+} + Ca^{2+} \pm \text{fluid} \leftrightarrow Si^{4+} + (Y + REE)^{3+} \pm \text{fluid}. \quad (3)$$

Fig. 10c illustrates the potential influence of reaction (3). Loss of Ca + P to apatite is balanced by enrichments in Y + Si + REEs in low-Ca monazite during fluid–rock interaction (e.g. Harlov et al., 2005). Domains 5–8 document this trend, being depleted in Ca + P and enriched in Si and LREEs relative to high-Ca Core Domains 1–4 (Fig. 10c; Table 3). Outermost rims and tips of Domain 8 are enriched in Ca + P and depleted in Y, Ce, Nd, Th, and Si relative to texturally adjoining regions of Domain 7 monazite in grains 1-m2 and 2-m1 (arrows in Fig. 10b and c; Table 3).

Natural and experimental data suggest that flattening of chondrite-normalized LREE patterns for peraluminous granites can be attributed to a decrease in the La/Sm ratio during progressive differentiation of the melt, synchronous with crystallization of monazite (Miller and Mittlefehldt, 1982; Rapp and Watson, 1986; Montel, 1993). Fig. 10d and e utilize the mole fraction of La/Sm in monazite as an index of REE-enrichment during crystallization to distinguish Domains 1 through 4. Compositions of Domain 2 monazite show a general evolution from the core outward, characterized by increasing La/Sm and decreasing cheralite component (arrows in Fig. 10d and e). The most LREE-depleted monazite domains in Fig. 10d and e correspond to Domain 2 outer cores. This result is inconsistent with crystallization of Domain 2 monazite in equilibrium with Domain 1 inner cores that are already LREE-enriched (e.g. Fig. 10d). Domain 3 monazite generally has the highest La/Sm ratios and/or the highest abundance of U, pointing to LREE-enrichment following resorption of Domain 2 monazite (Fig. 10d and e).

Domain 4, defined by the high-Ca core of grain 2-m1, is geochemically distinct from all other analyzed domains (Fig. 9a; #17 and #22 in Fig. 10, 11e). Core sub-domains analyzed in grain 2-m1 are enriched in U relative to all Domain 1 and 2 monazite (Fig. 10e). The resorbed inner core contains the highest amount of U (#22 in Fig. 10e; 1488 +/− 36 ppm: Table 3). The high-Ca overgrowth (#17 in Fig. 10e and 11e) is distinctly elevated in $LaPO_4$ + $CePO_4$ (in contrast to other Domain 2 monazite: 0.6410 vs. 0.6180–0.6307) and is the most enriched in Ce relative to all Domain 1–3 monazite (Table 3).

Trace element EPMA results validate the eight distinct domains identified in X-ray maps. Analysis of REE-enrichment in Fig. 10d and e is most consistent with resorption of early, LREE-enriched Domain 1

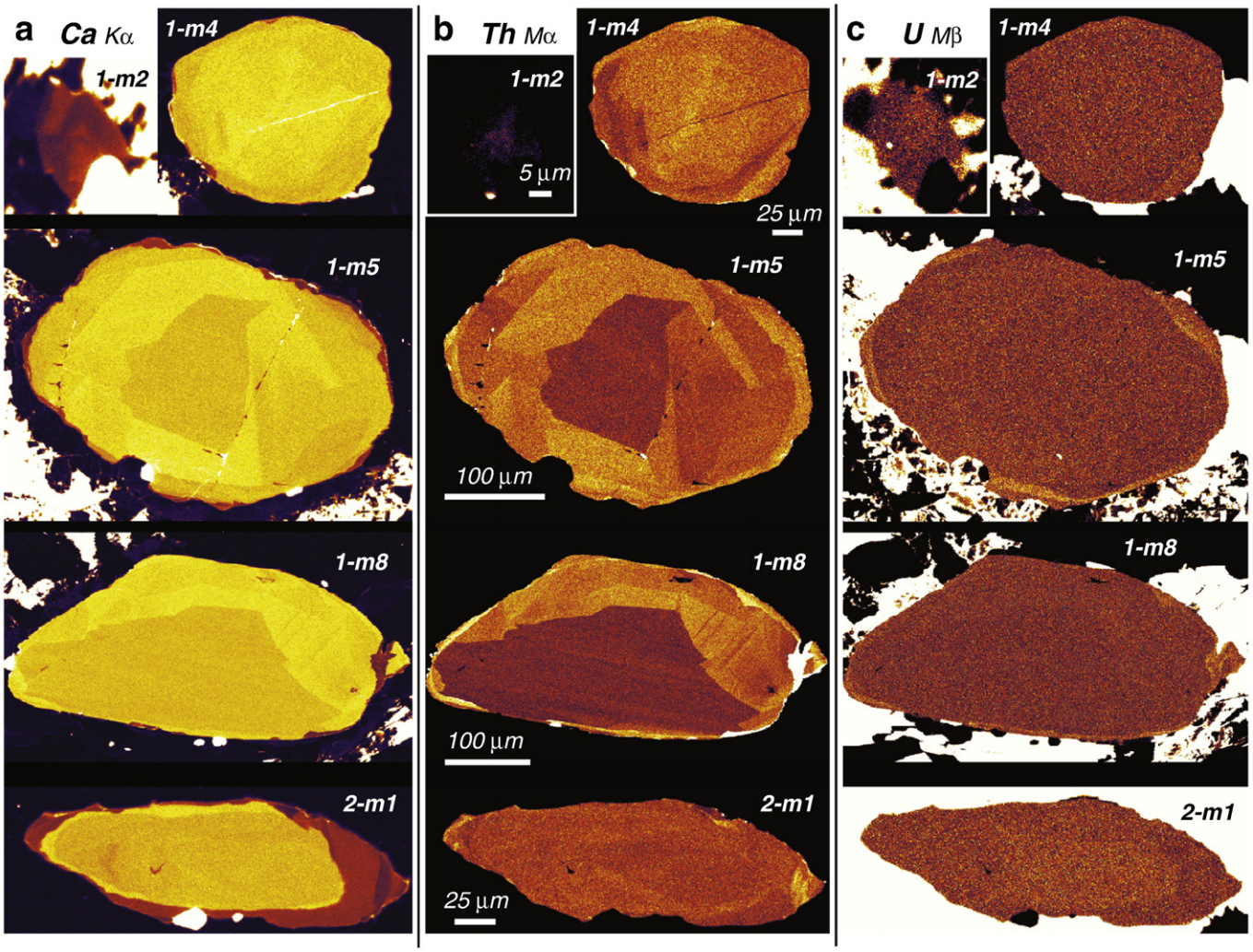

Fig. 8. Simultaneously processed high-resolution X-ray maps of a) Ca*Kα*, b) Th*Mα*, and c) U*Mβ* for grains 1-m2, 1-m4, 1-m5, 1-m8, and 2-m1 (i.e. all grains were mapped at the same analytical conditions, and the relative X-ray intensities are identical for all maps). Grain 1-m2 exhibits only the low-Ca domains due to a cut effect from successive grinding during polishing. Comparison of maps for Ca*Kα* and Th*Mα* suggests that the inner cores of grains 1-m5 and 1-m8 are compositionally similar. See Section 4.3.2. for discussion.

inner cores followed by crystallization of LREE-depleted Domain 2 outer cores. Progressive La/Sm enrichment and U-depletion of Domain 2 occurred prior to resorption of Domain 2 and growth of Domain 3. Domain 4, in the K-feldspar ribbon-hosted grain 2-m1 (Fig. 4e), remains distinct and cannot be wholly classified under any of the other seven compositional domains (Fig. 10e).

4.5. In situ EPMA monazite geochronology

In situ EPMA trace element data and calculated dates are summarized in Table 3 and Fig. 11. High-Ca cores (Domains 1–4) yield dates that range between 1934+/−19 Ma and 1903+/−22 Ma (2σ) (Fig. 11b–d). Dates for low-Ca rims (Domains 5–8) define two distinct populations at ca. 1850 Ma and ca. 1800 Ma (Figs. 3c, 11a, and d, e).

High-Ca Core Domains 1–4 are statistically indistinguishable at 95% confidence (Fig. 11a). Uncertainties (2σ) include a propagated 1% background uncertainty and are ± 15–25 Ma (Fig. 11a and Table 3). Weighted means, combining correlated domains from several monazite grains, are reported here based on the textural observations and geochemical data summarized in Sections 4.3 and 4.4 (Fig. 11a). The three dates acquired from inner cores of Domain 1 yield a weighted mean date of 1932±9 Ma (MSWD=2.6) for crystallization of early LREE-enriched monazite (Fig. 11a; inner cores plotted in Fig. 10b). All five dates obtained from Domain 2 outer cores (attributed to progressive LREE-enrichment during crystallization) yield a weighted mean date of 1923±8 Ma (MSWD=4.7) (Fig. 11a). Three dates for LREE-depleted Domain 2 outer core zones define a weighted mean date of 1921±11 Ma (MSWD=2.1) (Fig. 11a; analyses 3, 8, and 12 plotted in Fig. 10b, d, and e). Five dates for the high-U outermost zones of Domain 3 range between 1918±21 Ma and 1906±16 Ma (2σ), defining a weighted mean date of 1912±8 Ma (MSWD=2.2) (Fig. 11a). The distinct Domain 4 high-Ca core and overgrowth of grain 2-m1 yield dates of 1908±17 Ma and 1903±22 Ma (2σ), respectively (Fig. 11e).

Low-Ca rim Domains 5–7 define a single age population that is statistically different from Domains 1–4 and Domain 8 at 95% confidence. The five dates for low-Ca rims of Domains 5–7 define a weighted mean date of 1846±8 Ma (MSWD=1.1) (Fig. 11a). Two dates for the outermost tips of grains 1-m2 and 2-m1 (Domain 8: Fig. 10a–c) range from 1805±25 Ma to 1801±20 Ma (2σ) (Fig. 11a).

5. Discussion

The combined results support the following conceptual model (Fig. 12). Crystallization of igneous monazite and zircon was followed by at least three stages of sub-solidus monazite growth. The first stage is linked to regional *HP–HT* (high pressure–high temperature) metamorphism and deformation during dextral, strike–slip strain along the Grease River shear zone. The later two stages are interpreted

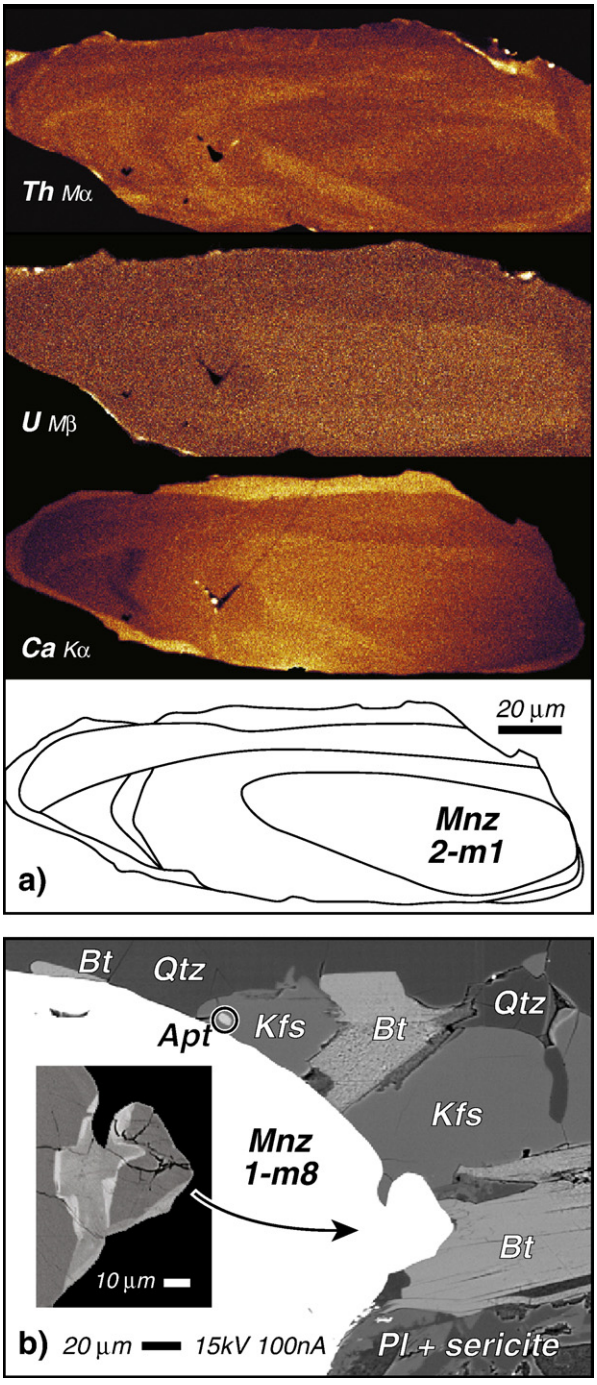

Fig. 9. a) Individually re-processed X-ray maps of Th*Mα*, U*Mβ*, and Ca*Kα* with sketch for the core of grain 2-m1 (compare to Fig. 8). b) Backscattered electron images illustrating microstructures and host matrix phases adjacent to right tip of grain 1-m8 in Fig. 7c. Note altered plagioclase at base of image and lobate intergrowth of K-feldspar near inset arrow. Inset shows high-contrast BSE image of right tip.

to record episodes of retrograde metamorphism and deformation during intra-continental shear zone reactivation and terrane uplift in the western Canadian Shield.

5.1. Magmatic co-crystallization of monazite and zircon in granite

Oscillatory- and sector-zoning observed in monazite (Domains 1 and 2) and in zircon imply crystallization in the presence of melt (e.g. Corfu et al., 2003). The weighted mean date for the three LREE-depleted Domain 2 outer cores (1921 ± 11 Ma) and the range of dates for all Domain 2 monazite (1927 ± 15 Ma to 1920 ± 18 Ma: Table 3) are statistically identical to the weighted mean ID-TIMS $^{207}Pb/^{206}Pb$ zircon date of 1922.6 ± 0.4 Ma (Fig. 11a). We interpret all of Domain 2 to be igneous monazite that co-crystallized with zircon from the parental dike melt.

Disparity in composition (Fig. 10b) and La/Sm enrichment (Fig. 10d and e) suggest that Domain 1 inner cores may represent early monazite that grew prior to melt extraction (Fig. 12a). These inner core domains may represent "restitic" Y-depleted, LREE-enriched monazite crystals that grew as a peritectic phase in the presence of melt + garnet during fluid-absent melting of biotite (e.g. Vielzeuf and Montel, 1994):

$$Bt_1 + Pl_1 + Qtz \rightarrow Grt + Kfs_1 + Melt + Mnz_{Domain1}, \quad (4)$$

consistent with the record of HREE-depletion indicated by whole rock geochemistry (Fig. 5; Table 1; mineral abbreviations after Bucher and Frey, 2002). Light REE-enriched Domain 1 monazite was subsequently entrained in the melt and underwent resorption during melt extraction (Fig. 12b). Complete dissolution of Domain 1 monazite prior to growth of Domain 2 was precluded by the large size of the domains (>200 μm), as supported by limited monazite diffusion modeling (i.e. Rapp and Watson, 1986). Subsequent igneous crystallization of LREE-depleted monazite Domain 2 was followed by renewed La/Sm enrichment during dike crystallization by a reaction such as:

$$Melt + Mnz_{Domain1} \rightarrow Bt_2 + Pl_2 + Kfs_2 + Qtz + Rt + Zrn + Mnz_{Domain2}. \quad (5)$$

(e.g. enrichment trends for 1-m4 and 1-m8 in Fig. 10d and e) (Fig. 12c) (i.e. Montel, 1993). Crystallization of monazite prior to zircon, as inferred above for monazite Domain 1, is well-established (e.g. Crowley et al., 2005; Kohn et al., 2005). However, the zircon dataset for 04G-019B does not preclude an older zircon component (e.g. oldest fraction L02c discussed in Section 4.1).

5.2. High-T, syn-kinematic recrystallization, dissolution, and re-precipitation of monazite in continental lower crust

Circa 1.0 GPa (~35-km paleodepth) exposures occur on both sides of the GRsz and in the vicinity of dike 04G-019B (Dumond et al., 2005; Williams and Hanmer, 2006), indicating a lower crustal level of dike emplacement at ca. 1923 Ma. Uranium- and LREE-enriched Domain 3 and 4 monazite yield dates that range between 1918 ± 18 Ma and 1903 ± 22 Ma. The dates overlap with the 1923 Ma igneous crystallization age for the dike and the ca. 1921–1896 Ma ages for granulite-facies deformation and *HP–HT* metamorphism documented throughout the Athabasca granulite terrane (Baldwin et al., 2003, 2004, 2006; Mahan et al., 2006a; Flowers et al., 2006a; Ashton et al., 2006; Martel et al., 2008; Mahan et al., in press; Flowers et al., in press).

Domains 3 and 4 are interpreted to reflect growth of monazite during high-*T* dextral shearing at lower crustal levels along the GRsz (Fig. 12d and e). Domain 1 and 2 cores are truncated by Domain 3 overgrowths that are aligned in the shear zone fabric (S_2 foliation) and generally have asymmetric 2-dimensional geometries compatible with top-to-the-NE dextral shear strain (e.g. Fig. 11b–e). The domains are interpreted to reflect the combined rotation and dissolution of igneous monazite grains (i.e. Domains 1 and 2) concurrent with preferential growth of Domain 3 monazite in dextral, top-to-the-NE extensional quadrants during general shear (Fig. 11b and c; i.e. Passchier and Trouw, 2005). The "mineral fish" geometry of Domain 4 is also consistent with dextral, top-to-the-NE strain. X-ray maps of the core of grain 2-m1 reveal internal Ca-, Th-, and U-zoning that is analogous to σ-type porphyroclasts characterized by successive "stair-stepping" overgrowths (Figs. 9a and 11e; i.e. Passchier and Trouw, 2005) and supporting a syn-kinematic interpretation for growth of Domain 4.

Many of the asymmetric grains are associated with or completely surrounded by dynamically recrystallized feldspar porphyroclasts and ribbons (Figs. 3a, 7, and 9b). The rotation and dissolution of Domains 1

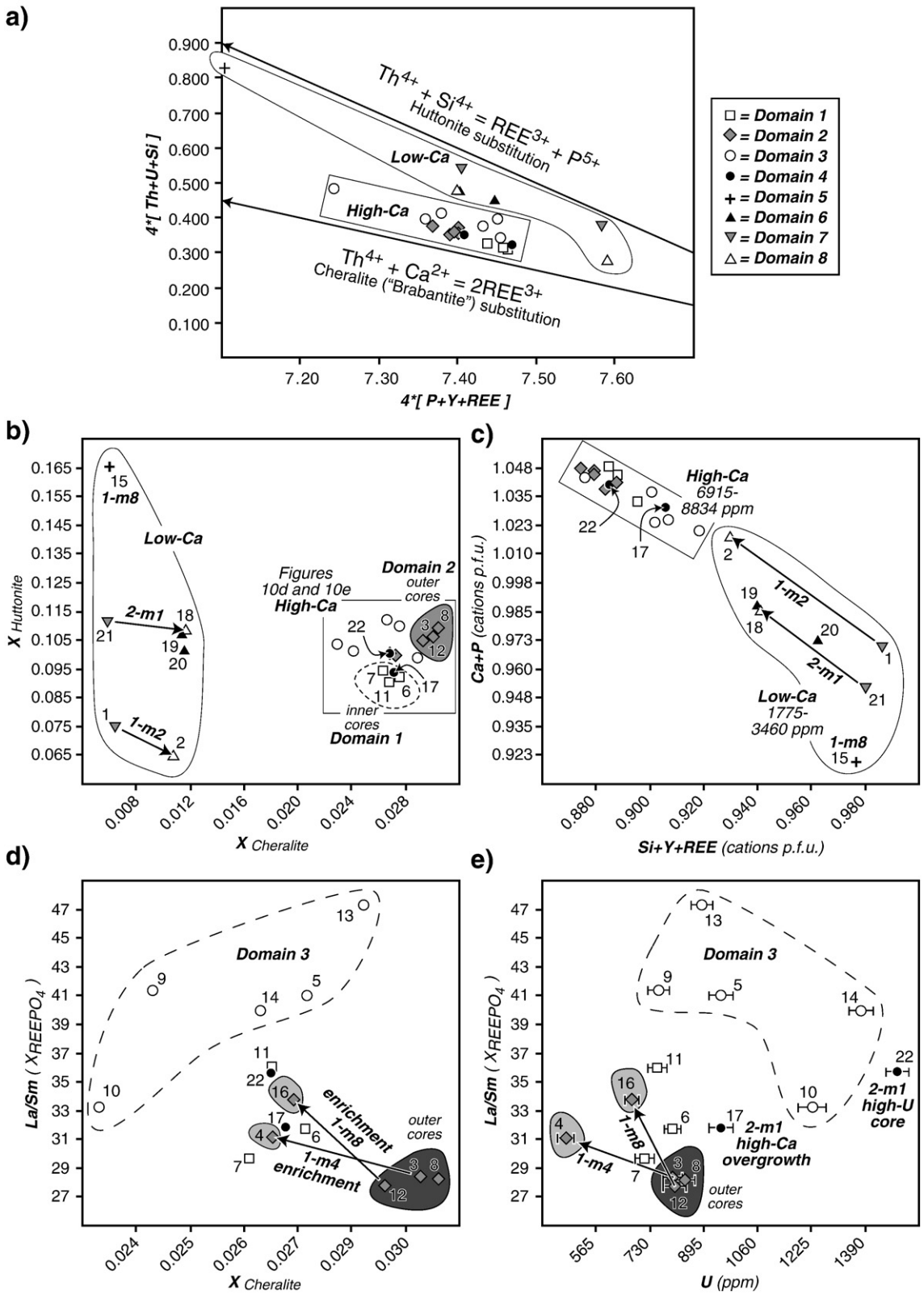

Fig. 10. a) Monazite cation plot normalized to 16 oxygens with arrows for end-member huttonite and cheralite (or 'brabantite') exchange vectors. Symbols are keyed to monazite compositional Domains 1–8 discussed in the text. b) Monazite component plot of $X_{Huttonite}$ vs. $X_{Cheralite}$ distinguishes data collected from low- and high-Ca domains highlighted by Ca*Kα* X-ray maps in Fig. 8a. Mole fractions for monazite components are calculated after Pyle et al. (2001). Fig. 10b can be considered an alternative to the more typical monazite exchange vector plot in Fig. 10a. c) Ca + P vs. Si + Y + REE (cations per forumula unit) illustrates an exchange mechanism that may control growth/dissolution of monazite + apatite in the presence of fluids (e.g. Harlov et al., 2005). d) La/Sm (X_{REEPO4}) vs. $X_{Cheralite}$. The La/Sm ratio serves as an index of REE-enrichment or fractionation during monazite crystallization from a peraluminous granite melt (i.e. Rapp and Watson, 1986; Montel, 1993). e) La/Sm (X_{REEPO4}) vs. U (ppm). See text and Section 4.4 for discussion. Note that numbered data points/symbols in all plots correspond to the location of analyzed domains in Fig. 11 and data in Table 3.

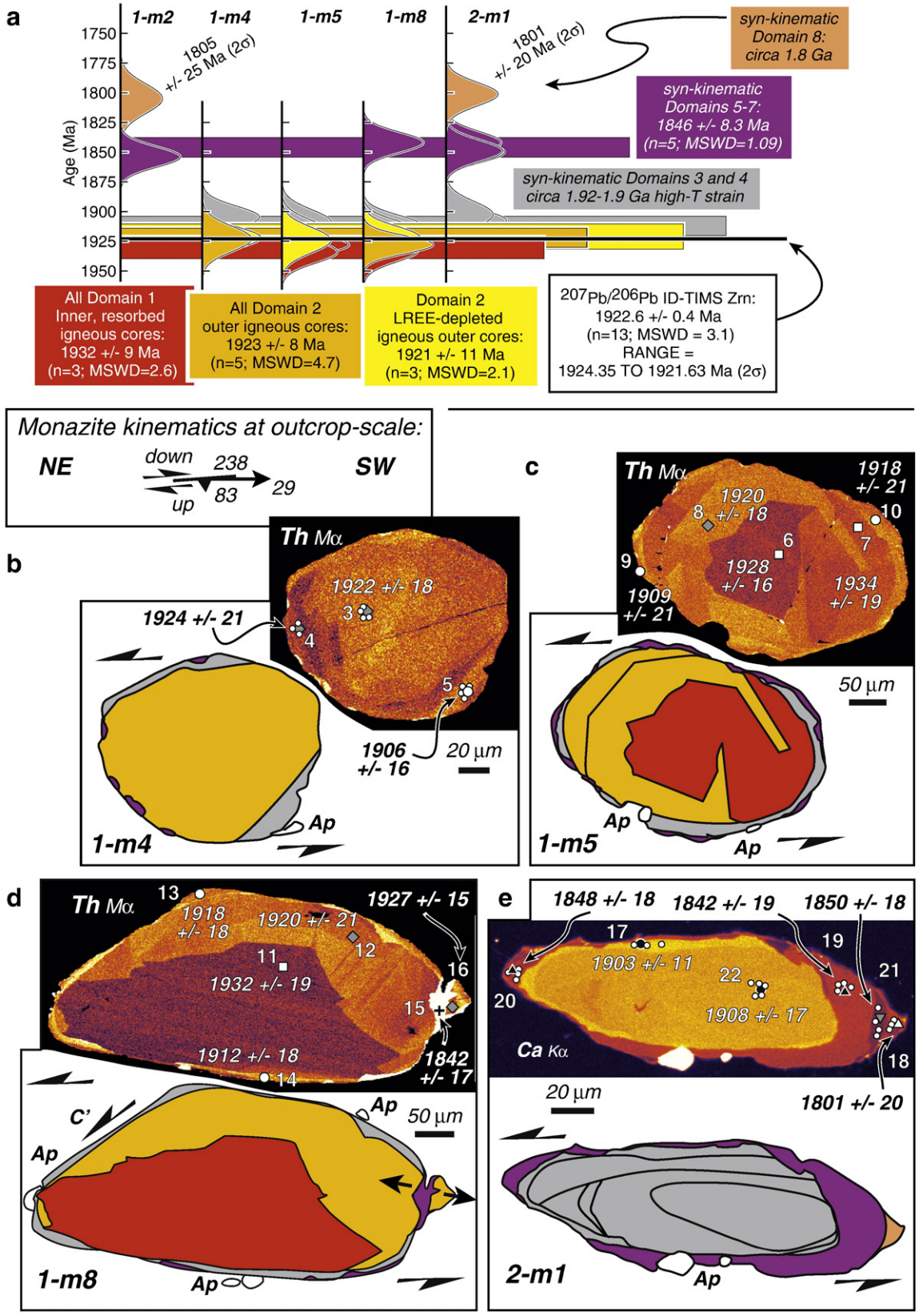

Fig. 11. a) Summary of all EPMA geochronologic data for monazite in dike 04G-019B. All histograms are scaled relative to the consistency standard in Fig. 3c. The black bar is scaled to show the range of dates for the thirteen zircon fractions analyzed by ID-TIMS (Fig. 6 and Table 2). Rationale behind weighted mean dates for the monazite data are discussed in Section 5. Dates are quoted at the 2σ level of uncertainty after Williams et al. (2006), including 1% uncertainty on the modeled background intensity. Note: Data for grain 1-m2 are illustrated in Fig. 3c, b–e) Representative maps, sketches of kinematic interpretations, and locations of EPMA trace element data. Ap = apatite. Locations of data acquisition points correspond to numbered data in Table 3 and domain symbols in Fig. 10. The size of the symbols in c) and d) is larger than the area of points used to analyze each domain as illustrated in b) and e).

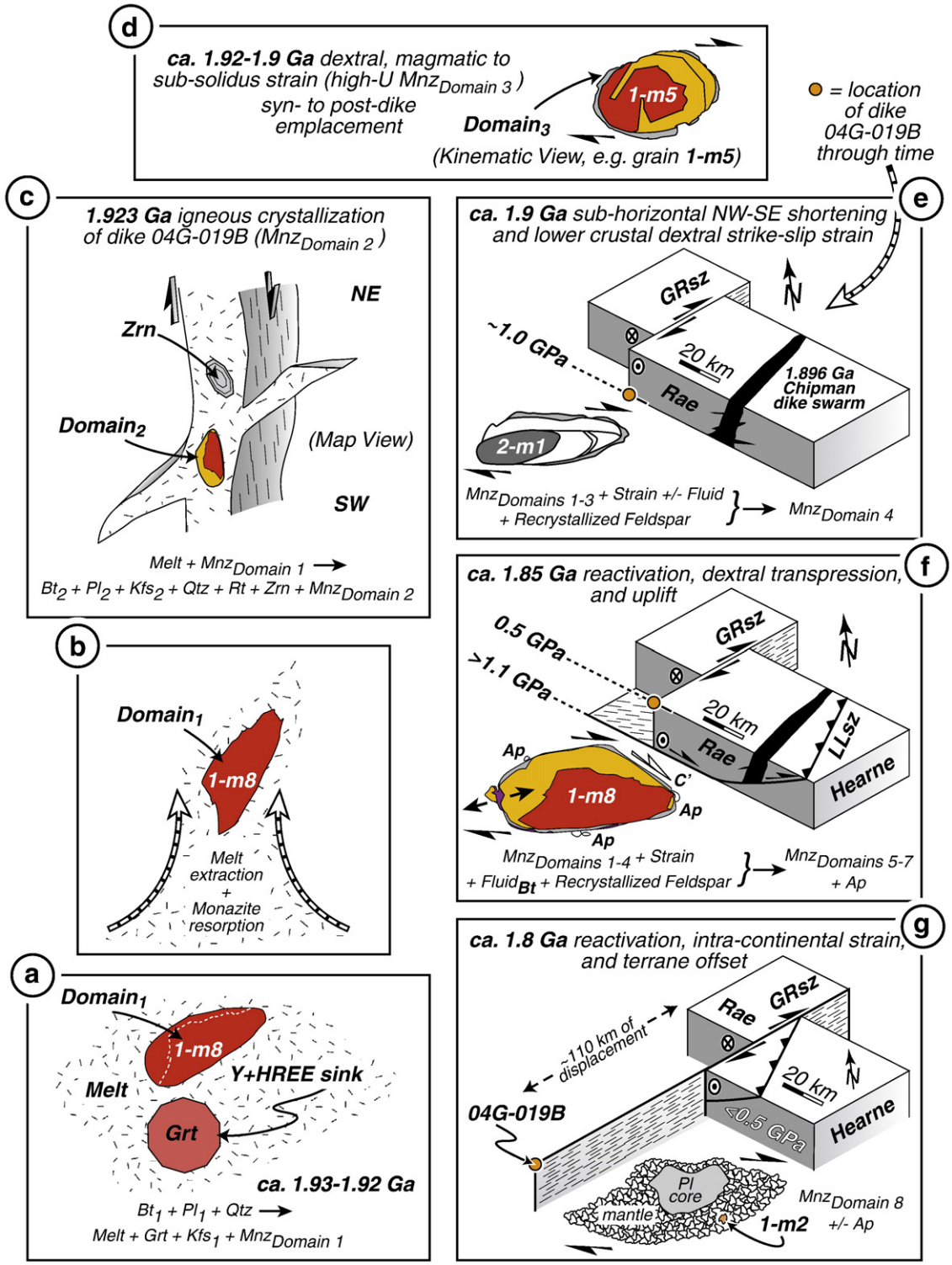

Fig. 12. Model for petrogenetic and deformation history recorded by accessory phases in dike 04G-019B. See Section 5 for discussion.

and 2, accompanied by the asymmetric growth of Domains 3 and 4, must have occurred during high-*T* magmatic to sub-solidus recrystallization of plagioclase+K-feldspar (i.e. feldspar ribbon development at ca. 650–750 °C: Tullis, 2002; Passchier and Trouw, 2005) (Fig. 4e). The geochemical characteristics of monazite Domains 3 and 4 may also indicate a transition from igneous to high-*T* sub-solidus growth. Resorption of Domains 1 and 2 followed by sharp overgrowths of U-rich Domain 3 is consistent with monazite dissolution and re-precipitation after magmatic zircon crystallization ceased, i.e. monazite became the dominant U-host during crystallization of the residual dike melt (e.g. grain 1-m5: Fig. 12d). This process would have been enhanced by metasomatic reactions involving alkali-rich fluids present during or after dike crystallization, such as:

$$(Na^+ + K^+ \text{ fluid}) \pm \text{residual melt} + Mnz_{Domains1-2} \rightarrow Mnz_{Domains3-4}. \quad (6)$$

Reaction (6) is suggested based on natural observations and experimental results that imply dissolution and re-precipitation of monazite is enhanced by the presence of alkal-rich fluids in the late

stages of granite pegmatite crystallization (Hetherington and Harlov, 2008). Furthermore, high-*T* feldspars are generally LREE-rich with high La/Sm ratios (Bea, 1996). The onset of Domain 3 growth generally coincides with distinct increases in both La/Sm ratios and La+Ce in monazite that we suggest reflects syn-kinematic growth during dynamic recrystallization of high-*T* igneous feldspars (Fig. 10d and e; Table 3).

We propose that Domains 3 and 4 represent a physical record of magmatic (1.923 Ga) to sub-solidus, high-*T* strain that lends support for syn-tectonic dike emplacement followed by protracted accumulation of dextral shear strain at ca. 1.92–1.9 Ga (Fig. 12d and e). It is likely that heat and fluids associated with dike emplacement served to enhance and localize deformation (i.e. Hollister and Crawford, 1986; Davidson et al., 1992). In situ dates for the core and rim of Domain 4 in grain 2-m1 bracket the age of at least one episode of high temperature K-feldspar recrystallization, ribbon development, and production of σ-type overgrowths of monazite in the GRsz to between 1908±17 Ma and 1903±22 Ma (2σ) (Figs. 11e and 12e).

5.3. Syn-kinematic, fluid-mediated growth of monazite+apatite in continental middle to upper crust

Previous petrologic and thermochronologic studies demonstrated that an important phase of uplift and exhumation in the region had occurred by 1.85 Ga (Mahan et al., 2006a; Flowers et al., 2006b). Multi-stage exhumation initiated shortly after lower crustal (1.0–1.1 GPa) emplacement of the 1.896 Ga Chipman amphibolite dike swarm (Fig. 12e; Flowers et al., 2006a,b). The thrust–sense Legs Lake shear zone is interpreted to have accommodated ~20 km of uplift and exhumation of the Athabasca granulite terrane to middle crustal levels (ca. 0.4–0.5 GPa) at ca. 1.85 Ga (Figs. 1b,c and 12f; Mahan et al., 2003, 2006a). The presence of similar high pressure (ca. 0.9–1.0 GPa) rocks along both sides of the strike–slip GRsz implies that dike 04G-019B was at similar middle crustal levels during growth of Domains 5–7 at ca. 1.85 Ga (Fig. 12f). The huttonitic character of Domain 5 monazite (Fig. 10a and b) supports this interpretation in light of recent experimental work suggesting that growth of huttonite on monazite substrates is apparently optimized at conditions of 500–700 °C and 0.5 GPa (Harlov et al., 2007).

Circa 1.85 Ga and 1.8 Ga Domains 5–8 involve relatively small amounts of monazite (Fig. 3), locally as tips, overgrowths, and fracture-fillings on pre-existing grains (e.g. Fig. 11b–e). The overgrowths occur along sharp, resorbed boundaries of early monazite, an observation that is consistent with the dissolution/re-precipitation mechanism inferred to explain experimentally-produced compositional zoning in monazite (e.g. Seydoux-Guillaume et al., 2002; Gardés et al., 2007; Harlov et al., 2007). Monazite Domains 5–8 are also distinctly lower in Ca+P (Fig. 10c) and contain the most elevated amounts of La+Ce (Table 3). These results (combined with textural observations of apatite+monazite, e.g. Figs. 3a, 7, 11b–e) are most consistent with inital growth of apatite at the expense of pre-existing monazite Domains 1–4 during recrystallization and alteration of LREE-enriched plagioclase+K-feldspar. The presence of secondary apatite (i.e. not as a primary igneous phase) and pervasive sericitization of feldspar near monazite grains indicates that fluids may have facilitated dissolution of high-Ca monazite and re-precipitation of low-Ca monazite+apatite. We favor an internal source of fluids based on observations of apatite intergrown with foliated biotite (e.g. Fig. 7c). Recrystallization of biotite would facilitate strain localization, liberation of water, and "hydrolytic weakening" (e.g. Post and Tullis, 1998; Holyoke and Tullis, 2006a,b) according to a reaction such as:

$$\text{Strain} + \text{Bt}_2 + \text{Pl}_2 + \text{Kfs}_2 + \text{Mnz}_{\text{Domain1–4}} \rightarrow \text{Fluid} + \text{Bt}_3 + \text{Pl}_3 + \text{Kfs}_3 + \text{Mnz}_{\text{Domains5–8}} + \text{Ap}. \quad (7)$$

Reaction (7) involves deformation-enhanced dissolution of pre-existing monazite Domains 1–4 and simultaneous precipitation of apatite and (Si+REE)-enriched monazite Domains 5–8 (Fig. 10c; see also Pan and Fleet, 2002; Harlov et al., 2005).

Recrystallization of biotite, coupled with alteration of plagioclase+K-feldspar, would promote the release of (K^++Na^+)-rich fluids that facilitate dissolution and re-precipitation of monazite (i.e. Hetherington and Harlov, 2008). Porosity development in phosphates (e.g. apatite: Dempster et al., 2006) and grain boundary migration of phases near phosphates are processes that would also enhance dissolution and re-precipitation mechanisms. Grain boundary migration recrystallization (GBMR: Passchier and Trouw, 2005) near monazite and apatite in 04G-019B is indicated by locally annealed foam texture in poly-crystalline mantles adjacent to feldspar porphyroclasts in Fig. 3a, abundant pinning microstructures defined by biotite+quartz in Fig. 7c, and the K-feldspar intergrowth with monazite Domain 5 in Fig. 9b.

Geochronology, microstructures, and compositional zoning require that all low-Ca monazite overgrowths developed during reactivation of gneissic fabric in the GRsz (e.g. Figs. 3a, 7, and 11b–e). Locally, there is a more brittle (i.e. lower-*T*) character to the microstructures as compared to earlier generations, e.g. monazite Domain 5 grew synchronous with brittle fracturing of grain 1-m8 (Figs. 9b, 11d, and 12f). Circa 1.85 Ga ages for syn-kinematic monazite growth in both the Grease River and Legs Lake shear zones provide the first compelling evidence for simultaneous slip along both structures during lower to middle crustal exhumation (Fig. 12f; Mahan et al., 2006a, and this study). The two structures were kinematically-linked during dextral transpression (e.g. Oldow et al., 1990), i.e. the strike–slip Grease River shear zone actively accommodated displacement in the hanging wall of the thrust–sense Legs Lake shear zone during emplacement of lower crust of the Rae domain over middle crust of the Hearne domain (Fig. 12f).

Additional regional exhumation of the Athabasca granulite terrane is interpreted to have occurred by 1.8 Ga (Flowers et al., 2006b). Circa 1.8 Ga monazite growth and shearing (as recorded in this dike and elsewhere: Hanmer et al., 1994; Williams and Jercinovic, 2002) occurred at shallower crustal levels (less than 0.4–0.5 GPa; Fig. 12g). The enrichment in Ca+P documented in Domain 8 relative to Domain 7 (Fig. 10c) may point to partial resorption of apatite during monazite growth at 1.8 Ga. This result would imply the reversal of reaction (3) during a ca. 1.8 Ga episode of strain-induced biotite recrystallization and renewed fluid–mineral interaction.

5.4. Tectonic implications for the western Canadian Shield — greater than 100 m.y. record for the Grease River shear zone

Results presented here suggest that the GRsz accommodated at least three episodes of dextral shear strain at ca. 1.92–1.9 Ga, ca 1.85 Ga. and ca 1.80 Ga. Rocks of the Athabasca granulite terrane were at lower crustal levels (ca. 1.0 GPa≈35–40 km depths) during the earliest phases of shearing at ca. 1.92–1.9 Ga (Fig. 12d and e). Tectonism at ca. 1.92–1.9 Ga is correlated regionally with the waning stages of arc-continent collision along the Taltson magmatic zone exposed in northeastern Alberta (Fig. 1a; McDonough et al., 2000) and contraction documented in the Snowbird Lake area of the Athabasca granulite terrane (Fig. 1b) (Martel et al., 2008). High pressure metamorphism at 1.9 Ga coincided with emplacement of the Chipman mafic dike swarm (Fig. 12e) (Flowers et al., 2006a). Circa 1.9 Ga displacement along the >400 km-long GRsz is interpreted as one manifestation of a continent-wide event in the western Canadian Shield, coinciding with dextral strike–slip displacement along the Great Slave Lake and Black Bay shear zones during collision of the Churchill and Slave cratons (Fig. 1a) (Bowring et al., 1984; Hoffman, 1987; Hanmer et al., 1992; Kraus and Ashton, 2000).

Circa 1.85 Ga movement along the GRsz was unknown prior to this study. Our results, in combination with data from Mahan et al. (2006a), provide the first evidence for simultaneous movement along the Grease River and Legs Lake shear zones at ca. 1.85 Ga. Mahan et al. (2003) documented ~20 km of vertical throw on the Legs Lake shear

zone, associated with uplift and exhumation of the Athabasca granulite terrane (Fig. 12f). Strike–slip reactivation of the GRsz in the hanging wall of the Legs Lake shear zone was temporally coincident with thrusting. Thus, the structural and monazite data provide kinematically- and geochronologically-compatible evidence for dextral transpression (i.e. "orogenic float" of Oldow et al., 1990: Fig. 12f).

Additional uplift and exhumation between 1.85 Ga and 1.8 Ga is indicated by field, petrologic, and geochronologic data (Mahan et al., 2006b; Flowers et al., 2006b). Movement on the GRsz at shallower crustal levels (less than 0.4–0.5 GPa) is supported by the presence of cataclasite, breccia zones, and pseudotachylite (Slimmon, 1989; Dumond and Goncalves, unpublished mapping; K. Bethune, personal communication). Circa 1.8 Ga reactivation along the GRsz coincides regionally with intra-continental strain observed throughout the western Churchill province and attributed to culmination of the Trans-Hudson orogeny (e.g. Aspler et al., 2002; Maclachlan et al., 2005; Ansdell, 2005; St-Onge et al., 2006). Our results support the interpretation of Mahan and Williams (2005) that ca. 1.8 Ga shearing along the GRsz facilitated the ~110 km of brittle–ductile offset of the Legs Lake shear zone, the Chipman dike swarm, and the Athabasca granulite terrane (Figs. 1b,c and 12g).

6. Conclusions and implications

The crustal-scale Grease River shear zone represents a long-lived tectonic discontinuity in the Canadian Shield. The structure was initiated as a ductile transcurrent zone in continental lower crust, and was active for >100 m.y. during multi-stage uplift and exhumation of the Athabasca granulite terrane and re-organization of the Laurentian supercontinent. It is not clear whether deformation in the shear zone was relatively continuous or restricted to three distinct episodes. The paucity of dates outside the three events identified here may imply a history of punctuated reactivation rather than prolonged periods of continuous movement.

Magmatic crystallization ages of cross-cutting igneous rocks are commonly regarded as strong constraints for bracketing the timing of deformation. In efforts to place tighter constraints on host rock deformation, igneous rocks that cut fabric (but also contain a deformational fabric) have been interpreted as syn-tectonic. Relative timing constraints, however, commonly involve significant assumptions in poly-deformed regions of continental crust. In situ monazite analysis by EPMA represents a powerful companion for U–Pb ID-TIMS geochronology with regard to timing fabric-forming events and illuminating otherwise unknown critical aspects of the tectonic history, such as the three post-igneous episodes documented in this study. The identification of eight texturally- and/or geochemically-distinct monazite generations emphasizes the importance of using high-resolution EPMA X-ray maps to guide precise trace element analysis. The results obtained in this study were gained by integrating compositional maps, trace element data, and Th–U–total Pb dates in the context of in situ microstructure to provide evidence for the production and repeated reactivation of gneissic fabric in a granitoid rock.

Monazite behaves like other porphyroclasts in granitic mylonites. More importantly, the microstructures and geometry of compositional domains can be used to directly link monazite generations to the timing of deformation fabrics. For igneous tectonites, syn-kinematic reactions involving Ca, P, and Si between monazite and apatite may prove just as useful as those reactions in metamorphic tectonites that utilize Y to establish links between monazite and garnet (e.g. Pyle and Spear, 2003; Gibson et al., 2004; Mahan et al., 2006a). Although Finger and Krenn (2007) emphasized the role of pre-existing apatite as a reactant accessory phase for the generation of polyphase monazite in high pressure granulite, we highlight the growth of apatite as a product phase during syn-kinematic monazite dissolution in lower crustal granite. This study illustrates that fluid-mediated, deformation-enhanced, dissolution and re-precipitation during dynamic recrystallization of monazite-bearing granite can be a powerful mechanism for directly linking μm-scale dissolution and re-precipitation to km-scale deformation events. Monazite provides a promising tool for timing shear zone evolution and rheologic behavior, particularly in light of recent work that emphasizes the role of deformation-enhanced reaction and fluid-liberation in experimentally deformed granitoids (Holyoke and Tullis, 2006a,b).

Acknowledgements

This research was funded by NSF-EAR grants 0310004 and 0609935 to M. Williams and S. Bowring. Additional support was provided by a 2005 Geological Society of America Graduate Student Research Grant to G. Dumond. The Department of Geosciences at UMass — Amherst provided additional field support to G. Dumond through the Leo Hall and Gloria Radke Memorial Funds. P. Goncalves is gratefully acknowledged for insightful discussion and outstanding field assistance during the initial outcrop discovery and extended field work in 2004 and 2005. K.H. Mahan is thanked for field assistance in 2006. The staff of Stony Rapids General Store is acknowledged for remarkable logistical support. Discussions with C. Hetherington, K. Mahan, B. Flowers, K. Bethune, B. Knox, K. Ashton, J. Crowley, S.A. Morse, S. Ascher, C. Clark, and Fr. D. McGonagle are greatly appreciated. We sincerely thank D. Harlov and F. Finger for patient encouragement and outstanding editorial assistance. K. Ashton is thanked for his encouraging support and a helpful informal review. Comments by two anonymous reviewers helped sharpen the presentation. One particularly critical anonymous review helped strengthen our resolve and our arguments.

Appendix A

Cameca® SX-100 "Ultrachron" EPMA analytical protocol for monazite trace element analysis with standard compositions utilized at the Univeristy of Massachusetts — Amherst Electron Microprobe/SEM Facility.

X-ray mapping sample conditions

Thin-sections were coated by vacuum thermal evaporation with ~250Å of carbon. Monazite grains in 04G-019B-1 were identified by stage-scan X-ray mapping of the entire thin-section at a rate of 60 ms/pixel in the Cameca® SX50 electron microprobe. Maps of raw X-ray counts for Ce$L\alpha$, P$K\alpha$, Zr$L\alpha$, and K$K\alpha$ (1024×512 pixel-size) were produced utilizing a 15 kV accelerating voltage with a 350 nA beam current, a defocused beam (~30–35 μm), and a 35 μm pixel-step size (Fig. 6a).

High-resolution X-ray maps for individual monazite grains were collected for Y$L\alpha$, Ca$K\alpha$, Th$M\alpha$, U$M\beta$, and Pb$M\alpha$ by stage-fixed beam-rastering or fixed-beam stage-scanning (0.3–6.0 μm pixel-step sizes at 80–100 ms/pixel) utilizing a focused beam at 15 kV and 200 nA (Fig. 7a).

Quantitative analysis sample conditions

Final thin-section preparation involved removal of the C-coat prior to 4–8 h of vibratory polishing with a colloidal silica suspension. Thin-sections and standards were loaded under high vacuum in a BOC Edwards Auto 306® vacuum coater, cleaned with plasma utilizing the Plasmaglo accessory, and simultaneously coated via high-precision vacuum thermal evaporation of ~200 Å Al followed by ~80Å C.

All quantitative analyses were carried out on the Cameca® "Ultrachron" electron microprobe outfitted with a LaB_6 source (Table 3). The instrument has five wavelength-dispersive spectrometers (WDS), two of which are "VL" spectrometers with Very Large PET crystals (2400 mm^2 in area) and detectors. The two VL spectrometers are simultaneously dedicated to analysis of Pb$M\alpha$. Count precision is increased by obtaining a weighted average of the K-ratio for Pb$M\alpha$ based on the net intensities (cts/s/nA) from both spectrometers (e.g. detection limits were 12–20 ppm for concentrations of 1470–8340 ppm Pb measured in this study; see Jercinovic et al., 2008-this

issue). A combination of natural and synthetic standards was used for calibration with a focused beam at 15 kV and 20 nA. Calibration and analysis of K$K\beta$ was carried out on the same spectrometer as U$M\beta$ to correct for the interference of K$K\alpha$ on U$M\beta$ that occurs in Mnz due to X-ray fluorescence within 10–15 μm of adjacent K-bearing phases (especially critical for monazite rim domains near K-feldspar and biotite in samples of this study: see Jercinovic and Williams, 2005).

Analytical points were chosen from homogeneous domains observed in high-resolution X-ray maps with emphasis placed on characterizing all observed textural/compositional variations in monazite, particularly domains with distinctive microstructures (e.g. Fig. 8a). For each domain, high-resolution WDS step scans of the background spectrum around Th$M\alpha$, U$M\beta$, and Pb$M\alpha$ were collected before each set of quantitative analyses at 15 kV and 200 nA with a focused beam. Raw background scans were converted to dead time-corrected, counts per second per nA and digitially-filtered prior to choosing regions of the curved background spectrum that avoided interferences. The selected background regions were regressed utilizing a best-fit exponential model to calculate the background intensity beneath each peak position for Th$M\alpha$, U$M\beta$, Pb$M\alpha$, and K$K\beta$ (see Jercinovic et al., 2008-this issue). Calibrated overlap correction factors for peak interferences of Y$L\gamma$ on Pb$M\alpha$, Th$M\zeta_1$ and Th$M\zeta_2$ on Pb$M\alpha$, 2nd order La$L\alpha$ on Pb$M\alpha$, Th$M\gamma$ on U$M\beta$, and K$K\alpha$ on U$M\beta$ were applied prior to ZAF corrections during the analytical sessions (see Donovan et al., 1993; Pyle et al., 2002, 2005; Jercinovic and Williams, 2005).

Analytical setup and standard compositions

WDS Spectrometer and signals used:

1 — PET: Si $K\alpha$, Y $L\alpha$, P $K\alpha$, Th $M\alpha$, Ca $K\alpha$
2 — LIF: As $K\alpha$, La $L\alpha$, Ce $L\alpha$, Pr Lβ, Nd $L\alpha$, Sm Lβ, Eu $L\alpha$, Gd Lβ, Tb $L\alpha$, Dy $L\alpha$, Ho Lβ, Er $L\alpha$, Tm $L\alpha$, Yb $L\alpha$
3 — VLPET: Pb $M\alpha$
4 — VLPET: Pb $M\alpha$
5 — LPET: U $M\beta$, K $K\beta$

Column conditions (LaB_6 source): 15 keV 200 nA (Focused beam at 10,000×)

Count times (seconds) on peak/background positions:

Si $K\alpha$=20/10
Y $L\alpha$=100/10
P $K\alpha$=20/10
Ca $K\alpha$=20/10
As $K\alpha$, La $L\alpha$, Ce $L\alpha$, Pr Lβ, Nd $L\alpha$, and Sm Lβ=20/10
Eu $L\alpha$ and Gd Lβ=40/20
Tb $L\alpha$, Dy $L\alpha$, Ho Lβ, Er $L\alpha$, Tm $L\alpha$, Yb $L\alpha$=20/10

Count times (seconds) on peak where modeled background is used to subtract the background intensity:

Th $M\alpha$=500
Pb $M\alpha$=600
U $M\beta$=500
K $K\beta$=100

Standards utilized:

Si, K Microcline (natural)
Y YAG (synthetic)
Pb Pyromorphite (natural)
U UO2 (synthetic, obtained from R. Ewing — University of Michigan)
(Synthetic REE-phosphates below obtained from J.-M. Montel, Laboratoire des Mécanismes et Transferts en Géologie, Université Paul-Sabatier; some synthesized by P. Goncalves — Université de Franche-Comté)
Yb YbPO4 (synthetic)
P, La LaPO4 (synthetic)
Th Brabantite2 (synthetic)
Ce CePO4 (synthetic)
Pr PrPO4 (synthetic)
Nd NdPO4 (synthetic)
Sm SmPO4 (synthetic)
Eu EuPO4 (synthetic)
Gd GdPO4 (synthetic)
Tb TbPO4 (synthetic)
Dy DyPO4 (synthetic)
Ho HoPO4 (synthetic)
Er Er (natural)
Tm Tm (natural)
As GaAs (natural)
Ca Wilberforce apatite (natural)

Standard compositions:

Microcline = O: 46.17%, Na: 0.97%, Mg: 0.02%, Al: 9.77%, Si: 30.3%, K: 12.68%, Ca: 0.01%, Ti: 0.01%, Mn: 0.03%, Fe: 0.03%
YAG = O: 32.34%, Al: 22.72%, Y: 44.94%
Pyromorphite = O: 14.85%, P: 6.87%, Cl: 2.62%, Pb: 76.23%
UO2 = U: 88.1495%, O: 11.8505%
LaPO4 = La: 59.392%, P: 13.2435%, O: 27.3645%
Brabantite2 = O: 28.126%, P: 13.356%, Ca: 8.026%, Th: 50.492%
GaAs = Ga: 48.208%, As: 51.792%
CePO4 = Ce: 59.6018%, P: 13.1751%, O: 27.2231%
PrPO4 = Pr: 59.7367%, P: 13.1311%, O: 27.1322%
NdPO4 = Nd: 60.2976%, P: 12.9482%, O: 26.7542%
SmPO4 = Sm: 61.2943%, P: 12.6231%, O: 26.0826%
EuPO4 = Eu: 61.5388%, P: 12.5434%, O: 25.9178%
GdPO4 = Gd: 62.3455%, P: 12.2803%, O: 25.3742%
TbPO4 = Tb: 62.594%, P: 12.1993%, O: 25.2068%
DyPO4 = Dy: 63.1133%, P: 12.0299%, O: 24.8568%
HoPO4 = Ho: 63.4582%, P: 11.9174%, O: 24.6244%
Er = Er: 100.%
Tm = Tm: 100.%
YbPO4 = Yb: 64.5639%, P: 11.5568%, O: 23.8793%
Wilberforce = O: 37.62%, F: 3.67%, Na: 0.18%, Mg: 0.02%, Si: 0.05%, P: 17.86%, S: 0.24%, Ca: 38.82%, Fe: 0.03%, Sr: 0.19%, Y: 0.03%, La: 0.11%, Ce: 0.24%.

References

Ansdell, K.M., 2005. Tectonic evolution of the Manitoba–Saskatchewan segment of the Paleoproterozoic Trans-Hudson Orogen, Canada. Canadian Journal of Earth Sciences 42 (4), 741–759.
Ansdell, K.M., Lucas, S.B., Connors, K.A., Stern, R.A., 1995. Kisseynew meta-sedimentary gneiss belt, Trans-Hudson orogen (Canada): back-arc origin and collisional inversion. Geology 23, 1039–1043.
Ashton, K.E., Knox, B., Bethune, K.M., Marcotte, J., 2006. Bedrock Geology along the Northern Margin of the Athabasca Basin West of Fond-du-Lac (NTS 74O-5 and -6), South-central Beaverlodge Domain, Rae Province, Fond-du-Lac Project. Summary of Investigations — Saskatchewan Geological Survey. Saskatchewan Industry and Resources, vol. 2, pp. 1–19.
Aspler, L.B., Chiarenzelli, J.R., McNicoll, V.J., 2002. Paleoproterozoic basement-cover infolding and thick-skinned thrusting in Hearne domain, Nunavut, Canada: intracratonic response to Trans-Hudson orogen. Precambrian Research 116 (3/4), 331.
Baldwin, J.A., Bowring, S.A., Williams, M.L., 2003. Petrological and geochronological constraints on high pressure, high temperature metamorphism in the Snowbird tectonic zone, Canada. Journal of Metamorphic Geology 21 (1), 81–98.

Baldwin, J.A., Bowring, S.A., Williams, M.L., Williams, I.S., 2004. Eclogites of the Snowbird tectonic zone: petrological and U–Pb geochronological evidence for Paleoproterozoic high-pressure metamorphism in the western Canadian Shield. Contributions to Mineralogy and Petrology 147 (5), 528–548.

Baldwin, J.A., Bowring, S.A., Williams, M.L., Mahan, K.H., 2006. Geochronological constraints on the evolution of high-pressure felsic granulites from an integrated electron microprobe and ID-TIMS geochemical study. Lithos 88 (1–4), 173–200.

Bea, F., 1996. Residence of REE, Y, Th, and U in granites and crustal protoliths: implications for the chemistry of crustal melts. Journal of Petrology 37, 521–552.

Berman, R.G., Davis, W.J., Pehrsson, S., 2007. Collisional Snowbird tectonic zone resurrected: Growth of Laurentia during the 1.9 Ga accretionary phase of the Hudsonian orogeny. Geology 35 (10), 911–914.

Berthé, D., Choukroune, P., Jegouzo, P., 1979. Orthogneiss, mylonite and non-coaxial deformation of granites: the example of the South Armorican Shear Zone. Journal of Structural Geology 1 (1), 31–42.

Bowring, S.A., Van Schmus, W.R., Hoffman, P.F., 1984. U–Pb zircon ages from Athapuscow aulacogen, East Arm of Great Slave Lake, N.W.T., Canada. Canadian Journal of Earth Sciences 21, 1315–1324.

Bucher, K., Frey, M., 2002. Petrogenesis of Metamorphic Rocks. Springer, Berlin.

Card, C.D., 2001. Basement rocks to the western Athabasca basin in Saskatchewan. Summary of Investigations — Saskatchewan Geological Survey. Saskatchewan Industry and Resources, vol. 2, pp. 321–333.

Card, C.D., 2006. Remote Predictive Map for the Basement to the Western Athabasca Basin, scale 1:500000. Open File 2006-45, Saskatchewan Industry and Resources.

Chacko, T., De, S.K., Creaser, R.A., Muehlenbachs, K., 2000. Tectonic setting of the Taltson magmatic zone at 1.9–2.0 Ga: a granitoid-based perspective. Canadian Journal of Earth Sciences 37, 1597–1609.

Cliff, R.A., Meffan-Main, S., 2003. Evidence from Rb–Sr microsampling geochronology for the timing of Alpine deformation in the Sonnblick Dome, SE Tauern Window, Austria. In: Vance, D., Muller, W., Villa, I.M. (Eds.), Geochronology: Linking the Isotopic Record with Petrology and Textures. The Geological Society, London, pp. 159–172.

Corfu, F., Hanchar, J.M., Hoskin, P.W.O., Kinny, P., 2003. Atlas of zircon textures. Reviews in Mineralogy and Geochemistry 53 (1), 469–500.

Crowley, J.L., Bowring, S.A., Searle, M.P., 2005. U–Th–Pb systematics of monazite, xenotime, and zircon from Pleistocene leucogranites at Nanga Parbat (Pakistan Himalaya), 15th Annual Goldschmidt Conference, Moscow, Idaho, USA: a voyage of discovery. Geochimica et Cosmochimica Acta 69 (10) Supplement 1, 15 May 2005, A8.

Davidson, C., Hollister, L.S., Schmid, S.M., 1992. Role of melt in the formation of a deep-crustal compressive shear zone: The Maclaren glacier metamorphic belt, south central Alaska. Tectonics 11 (2), 348–359.

Davis, W.J., Rayner, N., Williams, M.L., Jercinovic, M.J., Santos-Orestes, J., in review. Isotopic and trace element characterization of two new monazite megacryst standards for microbeam geochronological and geochemical analyses. Geostandards and Geoanalytical Research.

Dempster, T.J., Campanile, D., Holness, M.B., 2006. Imprinted textures on apatite: a guide to paleoporosity and metamorphic recrystallization. Geology 34 (11), 897–900.

Donovan, J.J., Snyder, D.A., Rivers, M.L., 1993. An improved interference correction for trace element analysis. Microbeam Analysis 2, 23–28.

Dumond, G., Goncalves, P., Williams, M.L., Bowring, S.A., 2005. Field-based constraints on lower crustal flow from the world's largest exposure of lower continental crust, Northern Saskatchewan, Canada. Eos Transactions of the American Geophysical Union — Fall Meeting Supplement 86 (52) Abstract V21A-0592.

Dumond, G., Goncalves, P., Mahan, K.H., McLean, N., Williams, M.L., Bowring, S.A., 2006. Minerals, mountains, and eleven orders of magnitude of intra-continental deformation: monazite in the context of metamorphic and igneous tectonites. Geological Society of America Abstracts with Programs 38 (7), 209.

Finger, F., Krenn, E., 2007. Three metamorphic monazite generations in a high-pressure rock from the Bohemian Massif and the potentially important role of apatite in stimulating polyphase monazite growth along a PT loop. Lithos 95 (1–2), 103–115.

Flowers, R., Bowring, S., Williams, M., 2006a. Timescales and significance of high-pressure, high-temperature metamorphism and mafic dike anatexis, Snowbird tectonic zone, Canada. Contributions to Mineralogy and Petrology 151 (5), 558–581.

Flowers, R.M., Mahan, K.H., Bowring, S.A., Williams, M.L., Pringle, M.S., Hodges, K.V., 2006b. Multistage exhumation and juxtaposition of lower continental crust in the western Canadian Shield: linking high-resolution U–Pb and $^{40}Ar/^{39}Ar$ thermochronometry with pressure–temperature-deformation paths. Tectonics 25 (TC4003). doi:10.1029/2005TC001912.

Flowers, R.M., Bowring, S., Mahan, K.H., Williams, M.L., in press. Craton stabilization and disruption from the lower crustal record in the western Canadian Shield. Contributions to Mineralogy and Petrology. doi:10.1007/s00410-008-0301-5.

Frost, B.R., Barnes, C.G., Collins, W.J., Arculus, R.J., Ellis, D.J., Frost, C.D., 2001. A geochemical classification for granitic rocks. Journal of Petrology 42 (11), 2033–2048.

Gardés, E., Montel, J.-M., Seydoux-Guillaume, A.-M., Wirth, R., 2007. Pb diffusion in monazite: new constraints from the experimental study of $Pb^{2+} \leftrightarrow Ca^{2+}$ interdiffusion. Geochimica et Cosmochimica Acta 71, 4036–4043.

Gibson, H.D., Carr, S.D., Brown, R.L., Hamilton, M.A., 2004. Correlations between chemical and age domains in monazite, and metamorphic reactions involving major pelitic phases: an integration of ID-TIMS and SHRIMP geochronology with Y–Th–U X-ray mapping. Chemical Geology 211 (3–4), 237–260.

Gower, R.J.W., Simpson, C., 1992. Phase boundary mobility in naturally deformed, high-grade quartzofeldspathic rocks: evidence for diffusional creep. Journal of Structural Geology 14, 301–314.

Gramaccioli, C.M., Segalstad, T.V., 1978. A uranium- and thorium-rich monazite from a south-alpine pegmatite at Piona, Italy. American Mineralogist 63, 757–761.

Hajnal, Z., Lewry, J., White, D., Ashton, K., Clowes, R., Stauffer, M., Gyorfi, I., Takacs, E., 2005. The Sask Craton and Hearne Province margin: seismic reflection studies in the western Trans-Hudson Orogen. Canadian Journal of Earth Sciences 42 (4), 403–419.

Hanmer, S., 1994. Geology, East Athabasca mylonite triangle, Saskatchewan: Map 1859A, scale 1:100000. Geological Survey of Canada.

Hanmer, S., Bowring, S.A., Van Breeman, O., Parrish, R.R., 1992. Great Slave Lake shear zone, northwest Canada: mylonitic record of Early Proterozoic convergence, collision, and indentation. Journal of Structural Geology 14, 757–773.

Hanmer, S., Parrish, R.R., Williams, M.L., Kopf, C., 1994. Striding-Athabasca mylonite zone: complex Archean deep crustal deformation in the East Athabasca mylonite triangle, N. Saskatchewan. Canadian Journal of Earth Sciences 31, 1287–1300.

Harlov, D.E., Wirth, R., Förster, H.-J., 2005. An experimental study of dissolution–reprecipitation in fluorapatite: fluid infiltration and the formation of monazite. Contributions to Mineralogy and Petrology 150 (3), 268–286.

Harlov, D.E., Wirth, R., Hetherington, C.J., 2007. The relative stability of monazite and huttonite at 300–900 °C and 200–1000 MPa: metasomatism and the propagation of metastable mineral phases. American Mineralogist 92, 1652–1664.

Hartlaub, R.P., Chacko, T., Heaman, L.M., Creaser, R.A., Ashton, K.E., Simonetti, A., 2005. Ancient (Meso- to Paleoarchean) crust in the Rae Province, Canada: evidence from Sm–Nd and U–Pb constraints. Precambrian Research 141, 137–153.

Hetherington, C.J., Harlov, D.E., 2008. Metasomatic thorite and uraninite inclusions in xenotime and monazite from granitic pegmatites, Hidra anorthosite massif, southwestern Norway: mechanics and fluid chemistry. American Mineralogist 93, 806–820.

Hoffman, P.F., 1987. Continental transform tectonics; Great Slave Lake shear zone (ca. 1.9 Ga), Northwest Canada. Geology 15 (9), 785–788.

Hoffman, P.F., 1988. United Plates of America, the birth of a craton: Early Proterozoic assembly and growth of Laurentia. Annual Review of Earth & Planetary Sciences 16, 543–603.

Hollister, L.S., Crawford, M.L., 1986. Melt-enhanced deformation; a major tectonic process. Geology 14 (7), 558–561.

Holyoke III, C.W., Tullis, J., 2006a. Formation and maintenance of shear zones. Geology 34 (2), 105–108.

Holyoke III, C.W., Tullis, J., 2006b. The interaction between reaction and deformation: an experimental study using a biotite+plagioclase+quartz gneiss. Journal of Metamorphic Geology 24 (8), 743–762.

Jaffey, A.H., Flynn, K.F., Glendenin, L.E., Bentley, W.C., Essling, A.M., 1971. Precision measurement of half-lives and specific activities of ^{235}U and ^{238}U. Physical Review C 4 (5), 1889–1906.

Jercinovic, M.J., Williams, M.L., 2005. Analytical perils (and progress) in electron microprobe trace element analysis applied to geochronology: background acquisition, interferences, and beam irradiation effects. American Mineralogist 90 (4), 526–546.

Jercinovic, M.J., Williams, M.L., Lane, E.D., 2008. In situ trace element analysis in complex, multi-phase materials by EPMA. Chemical Geology 254, 197–215 (this issue). doi:10.1016/j.chemgeo.2008.05.016.

Jessell, M.W., 1987. Grain-boundary migration microstructures in a naturally deformed quartzite. Journal of Structural Geology 9, 1007–1014.

Kohn, M.J., Wieland, M.S., Parkinson, C.D., Upreti, B.N., 2005. Five generations of monazite in Langtang gneisses: implications for chronology of the Himalayan metamorphic core. Journal of Metamorphic Geology 23 (5), 399–406.

Kraus, J., Ashton, K.E., 2000. New insights into the structural geology and tectonic setting of the Uranium City area, northwestern Saskatchewan. Summary of Investigations — Saskatchewan Geological Survey. Saskatchewan Industry and Resources, vol. 2, pp. 16–25.

Krogh, T.E., 1973. A low contamination method for the hydrothermal decomposition of zircon and extraction of U and Pb for isotopic age determinations. Geochimica Cosmochimica et Acta 37, 485–494.

Krogh, T.E., 1982. Improved accuracy of U–Pb zircon ages by the creation of more concordant systems using an air abrasion technique. Geochimica Cosmochimica et Acta 46, 637–649.

LaFrance, B., Sibbald, T.I.I., 1997. The Grease River shear zone: Proterozoic overprinting of the Archean Tantato domain. Summary of Investigations — Saskatchewan Geological Survey, Saskatchewan Industry and Resources, pp. 132–135.

MacLachlan, K., Davis, W.J., Relf, C., 2005. Paleoproterozoic reworking of an Archean thrust fault in the Hearne domain, Western Churchill Province: U–Pb geochronological constraints. Canadian Journal of Earth Sciences 42 (7), 1313–1330.

Mahan, K.H., Williams, M.L., 2005. Reconstruction of a large deep-crustal terrane: implications for the Snowbird tectonic zone and early growth of Laurentia. Geology 33 (5), 385–388.

Mahan, K.H., Williams, M.L., Baldwin, J.A., 2003. Contractional uplift of deep crustal rocks along the Legs Lake shear zone, western Churchill Province, Canadian Shield. Canadian Journal of Earth Sciences 40 (8), 1085–1110.

Mahan, K.H., Goncalves, P., Williams, M.L., Jercinovic, M.J., 2006a. Dating metamorphic reactions and fluid flow: application to exhumation of high-P granulites in a crustal-scale shear zone, western Canadian Shield. Journal of Metamorphic Geology 24 (3), 193–217.

Mahan, K.H., Williams, M.L., Flowers, R.M., Jercinovic, M.J., Bowring, S.A., Baldwin, J.A., 2006b. Geochronological constraints on the Legs Lake shear zone with implications for regional exhumation of lower continental crust, western Churchill Province, Canadian Shield. Contributions to Mineralogy and Petrology 152 (2), 223–242.

Mahan, K.H., Goncalves, P., Flowers, R.M., Williams, M.L., Hoffman-Setka, D., in press. The role of heterogeneous strain in the development and preservation of a polymetamorphic record in high-P granulites, western Canadian Shield. Journal of Metamorphic Geology. doi:10.1111/j.1525-1314.2008.00783.x.

Mancktelow, N.S., 2006. How ductile are ductile shear zones? Geology 34 (5), 345–348.

Martel, E., van Breemen, O., Berman, R.G., Pehrsson, S., 2008. Geochronology and tectonometamorphic history of the Snowbird Lake area, Northwest Territories, Canada: new insights into the architecture and significance of the Snowbird tectonic zone. Precambrian Research 161, 201–230.

Mattinson, J.M., 2005. Zircon U–Pb chemical abrasion ("CA-TIMS") method: Combined annealing and multi-step partial dissolution analysis for improved precision and accuracy of zircon ages. Chemical Geology 220 (1/2), 47–66.

McDonough, W.F., Sun, S.-s., 1995. The composition of the Earth. Chemical Geology 120, 223–253.

McDonough, M.R., McNicoll, V.J., Schetselaar, E.M., Grover, T.W., 2000. Geochronological and kinematic constraints on crustal shortening and escape in a two-sided oblique-slip collisional and magmatic oroge, Paleoproterozoic Taltson magmatic zone, northeastern Alberta. Canadian Journal of Earth Sciences 37 (11), 1549–1573.

Miller, C.F., Mittlefehldt, D.W., 1982. Depletion of rare-earth elements in felsic magmas. Geology 10, 129–133.

Montel, J.-M., 1993. A model for monazite/melt equilibrium and application to the generation of granitic magmas. Chemical Geology 110 (1–3), 127–146.

Montel, J.-M., Foret, S., Veschambre, M., Nicollet, C., Provost, A., 1996. Electron microprobe dating of monazite. Chemical Geology 131 (1–4), 37–53.

Murphy, M.A., Copeland, P., 2005. Transtensional deformation in the central Himalaya and its role in accommodating growth of the Himalayan orogen. Tectonics 24 (TC4012). doi:10.1029/2004TC001659.

Oldow, J.S., Bally, A.W., Ave Lallemant, H.G., 1990. Transpression, orogenic float, and lithospheric balance. Geology 18 (10), 991–994.

Pan, Y., Fleet, M.E., 2002. Composition of the apatite-group minerals: substitution mechanisms and controlling factors. In: Kohn, M.J., Rakovan, J., Hughes, J.M. (Eds.), Reviews in Mineralogy and Geochemistry. Mineralogical Society of America, Washington, D.C., pp. 13–49.

Passchier, C.W., Trouw, R.A.J., 2005. Micro-tectonics, 2nd edition. Springer, Berlin.

Paterson, S.R., Tobisch, O.T., 1988. Using pluton ages to date regional deformations: problems with commonly used criteria. Geology 16, 1108–1111.

Paterson, S.R., Vernon, R.H., Tobisch, O.T., 1989. A review of criteria for the identification of magmatic and tectonic foliations in granitoids. Journal of Structural Geology 11, 349–363.

Percival, J.A., West, G.F., 1994. The Kapuskasing uplift: a geological and geophysical synthesis. Canadian Journal of Earth Sciences 31, 1256–1286.

Post, A., Tullis, J., 1998. The rate of water penetration in experimentally deformed quartzite: implications for hydrolytic weakening. Tectonophysics 295, 117–137.

Pyle, J.M., Spear, F.S., 2003. Four generations of accessory-phase growth in low-pressure migmatites from SW New Hampshire. American Mineralogist 88, 338–351.

Pyle, J.M., Spear, F.S., Rudnick, R.L., McDonough, W.F., 2001. Monazite–xenotime–garnet equilibrium in metapelites and a new monazite–garnet thermometer. Journal of Petrology 42 (11), 2083–2107.

Pyle, J.M., Spear, F.S., Wark, D.A., 2002. Electron microprobe analysis of REE in apatite, monazite, and xenotime: protocols and pitfalls. In: Kohn, M.J., Rakovan, J., Hughes, J.M. (Eds.), Reviews in Mineralogy and Geochemistry. Mineralogical Society of America, Washington, D.C., pp. 337–362.

Pyle, J.M., Spear, F.S., Wark, D.A., Daniel, C.G., Storm, L.C., 2005. Contributions to precision and accuracy of chemical ages of monazite. American Mineralogist 90, 547–577.

Rainbird, R.H., Stern, R.A., Rayner, N., Jefferson, C.W., 2007. Age, provenance, and regional correlation of the Athabasca Group, Saskatchewan and Alberta, constrained by igneous and detrital zircon geochronology. In: Jefferson, C.W., Delaney, G. (Eds.), EXTECH IV: Geology and Uranium EXploration TECHnology of the Proterozoic Athabasca Basin, Saskatchewan and Alberta. Bulletin, vol. 588. Geological Survey of Canada, pp. 193–209.

Rapp, R.P., Watson, E.B., 1986. Monazite solubility and dissolution kinetics: implications for the Th and light rare-earth chemistry of felsic magmas. Contributions to Mineralogy and Petrology 94, 304–316.

Ross, G.M., 2002. Evolution of Precambrian continental lithosphere in Western Canada: results from Lithoprobe studies in Alberta and beyond. Canadian Journal of Earth Sciences 39 (3), 413–437.

Schmitz, M.D., Schoene, B., 2007. Derivation of isotope ratios, errors, and error correlations for U–Pb geochronology using ^{205}Pb–^{235}U–(^{233}U)-spiked isotope dilution thermal ionization mass spectrometric data. Geochemistry Geophysics Geosystems 8 (Q08006). doi:10.1029/2006GC001492.

Schoene, B., Crowley, J.L., Condon, D.J., Schmitz, M.D., Bowring, S.A., 2005. Reassessing the uranium decay constants for geochronology using ID-TIMS U–Pb data. Geochimica et Cosmochimica Acta 70, 426–445.

Seydoux-Guillaume, A.-M., Paquette, J.-L., Wiedenbeck, M., Montel, J.-M., Heinrich, W., 2002. Experimental resetting of the U–Th–Pb systems in monazite. Chemical Geology 191 (1–3), 165–181.

Shaw, C.A., Karlstrom, K.E., Williams, M.L., Jercinovic, M.J., McCoy, A.M., 2001. Electron-microprobe monazite dating of ca. 1.71–1.63 Ga and ca. 1.45–1.38 Ga deformation in the. Geology 29 (8), 739–742.

Slimmon, W.L., 1989. Bedrock compilation geology — Fond du Lac (NTS 74-O): Map 247A, scale 1:250000. Saskatchewan Geological Survey, Saskatchewan Energy and Mines.

Spear, F.S., Pyle, J.M., 2002. Apatite, monazite, and xenotime in metamorphic rocks. In: Kohn, M.J., Rakovan, J., Hughes, J.M. (Eds.), Reviews in Mineralogy and Geochemistry. Mineralogical Society of America, Washington, D.C., pp. 293–335.

St-Onge, M.R., Searle, M.P., Wodicka, N., 2006. Trans-Hudson Orogen of North America and Himalaya–Karakoram–Tibetan Orogen of Asia: structural and thermal characteristics of the lower and upper plates. Tectonics 25 (TC4006). doi:10.1029/2005TC001907.

Tella, S., Hanmer, S., Ryan, J.J., Sandeman, H.A., Davis, W.J., Berman, R., Wilkinson, L., Mills, A., 2000. 1:100000 scale bedrock geology compilation map of the MacQuoid Lake-Gibson Lake-Cross Bay-Akunak Bay region, western Churchill province, Nunavut, Canada. Geological Association of Canada—Mineralogical Association of Canada Program with Abstracts, 25: Conference CD 676.

Teyssier, C., 1985. A crustal thrust system in an intra-cratonic environment. Journal of Structrual Geology 7, 689–700.

Tullis, J., 2002. Deformation of granitic rocks: experimental studies and natural examples. In: Karato, S., Wenk, H.-R. (Eds.), Reviews in Mineralogy and Geochemistry. Mineralogical Society of America, Washington, D.C., pp. 51–96.

van Breeman, O., Harper, C.T., Berman, R.G., Wodicka, N., 2007a. Crustal evolution and Neoarchean assembly of the central-southern Hearne domains: Evidence from U–Pb geochronology and Sm–Nd isotopes of the Phelps Lake area, northeastern Saskatchewan. Precambrian Geology 159, 33–59.

van Breeman, O., Pehrsson, S., Peterson, T.D., 2007b. Reconnaissance U–Pb SHRIMP geochronology and Sm–Nd isotope analyses from the Tehery-Wager Bay gneiss domain, western Churchill Province, Nunavut. Geological Survey of Canada, Current Research 2007- F2.

Vielzeuf, D., Montel, J.M., 1994. Partial melting of metagreywackes. Part I. Fluid-absent experiments and phase relationships. Contributions to Mineralogy and Petrology 117 (4), 375–393.

Whitmeyer, S.J., Karlstrom, K.E., 2007. Tectonic model for the Proterozoic growth of North America. Geosphere 3 (4), 220–259.

Williams, M.L., Jercinovic, M.J., 2002. Microprobe monazite geochronology: putting absolute time into microstructural analysis. Journal of Structural Geology 24 (6/7), 1013–1028.

Williams, M.L., Hanmer, S., 2006. Structural and metamorphic processes in the lower crust: evidence from a deep-crustal isobarically cooled terrane, Canada. In: Brown, M., Rushmer, T. (Eds.), Evolution and Differentiation of the Continental Crust. Cambridge University Press, Cambridge, pp. 231–267.

Williams, M.L., Hanmer, S., Kopf, C., Darrach, M., 1995. Syntectonic generation and segregation of tonalitic melts from amphibolite dikes in the lower crust, Striding-Athabasca mylonite zone, northern Saskatchewan. Journal of Geophysical Research 100 (B8), 15717–15734.

Williams, M.L., Melis, E.A., Kopf, C., Hanmer, S., 2000. Microstructural tectonometamorphic processes and the development of gneissic layering: a mechanism for metamorphic segregation. Journal of Metamorphic Geology 18 (41–57).

Williams, M.L., Jercinovic, M.J., Goncalves, P., Mahan, K., 2006. Format and philosophy for collecting, compiling, and reporting microprobe monazite ages. Chemical Geology 225 (1/2), 1–15.

Williams, M.L., Jercinovic, M.J., Hetherington, C.J., 2007. Microprobe monazite geochronology: understanding geologic processes by integrating composition and chronology. Annual Review of Earth & Planetary Sciences 35, 137–175.

Zhu, X.K., O'Nion, R.K., 1999. Zonation of monazite in metamorphic rocks and its implications for high temperature thermochronology: a case study from the Lewisian terrain. Earth and Planetary Science Letters 171, 209–220.